UNIVERSITÀ DEGLI STUDI ROMA TRE

Dipartimento di Matematica e Fisica
Corso di Laurea in Fisica

Tesi di Laurea Magistrale

# Towards electric and optical control of erbium Rydberg atoms

Laureando

**Marco Lucibello**
Matricola 559776

| Relatore interno | Relatore |
|---|---|
| **Prof. Marco Barbieri** | **Univ. Prof. Dr. Francesca Ferlaino** |

Anno Accademico 2024/25

*To my family*

# Contents

# Introduction

The manipulation of ultracold atomic gases has opened new frontiers in experimental quantum physics, enabling the realization of highly controllable platforms for studying complex quantum phenomena [1, 2, 3]. Since the first observation of Bose–Einstein condensates (BECs) [4, 5, 6] and degenerate Fermi gases [7], the field has rapidly advanced towards the development of quantum simulators based on optical tweezer arrays [8, 9, 10]. In particular, the excitation of atoms to Rydberg states provides strong and long-range interactions, making these platforms ideally suited for investigating quantum magnetism, Ising-type models, and other many-body phenomena beyond the reach of classical computation [11, 12, 13, 14].

A key requirement for such experiments is the ability to precisely control both the internal and external degrees of freedom of the atoms. Due to their exaggerated polarizabilities, Rydberg states are extremely sensitive to static and dynamic electric fields, which can significantly shift their energies (Stark effect) and modify their interactions [15, 16]. Accurate characterization and active stabilization of the electric field environment are therefore essential for the reliable operation of quantum simulators based on Rydberg atoms.

For complex atomic species such as the lanthanides — and erbium (Er) in particular — the rich electronic structure with multiple optical transitions, including narrow-line transitions, allows laser cooling into the microkelvin regime [17, 18, 19]. In addition, laser cooling techniques have made it possible to reduce the atomic temperature well below the Doppler limit [20, 21], giving access to sub-Doppler regimes that are crucial for improved control of atoms in optical tweezers.

The work presented in this thesis is situated within this framework. The long-term goal of the experiment is to realize a quantum simulator with erbium atoms trapped in two-dimensional optical tweezer arrays generated by a spatial light modulator (SLM). In particular, my contribution focuses on two fundamental aspects: (i) the implementation and characterization of electric field control inside the experimental chamber, and (ii) the first steps towards sub-Doppler cooling strategies, aiming to reduce the atomic temperature for subsequent quantum manipulation.

The thesis is structured as follows:

**Chapter 1** provides an introduction to the physics of Rydberg atoms with a particular focus on erbium as the atomic species of choice for our experiment. We also describe how to excite a Rydberg state using a two-photon transition, keeping coherent oscillations between the ground and the Rydberg state.

**Chapter 2** presents the design and implementation of the experimental setup for electric field control. We describe the electrodes configuration and the associated driving electronics.

**Chapter 3** reports the experimental results obtained with the electrodes. We emphasize the importance of electric field compensation for quantum simulations, due to the extraordinary sensitivity of Rydberg atoms to stray fields. The discussion includes measurements related to the compensation procedure and the determination of the static polarizability of the $47s$ Rydberg state of erbium.

**Chapter 4** addresses the motivation and first experimental steps towards sub-Doppler cooling of erbium. We discuss why reaching lower temperatures is essential for the success of future experiments, focusing on the implementation of cooling on the narrow 841 nm transition. Possible improvements and future directions are outlined.

# Chapter 1

# Rydberg Atoms

In this Chapter, we provide a general overview of Rydberg atoms, which are one of natures most versatile quantum systems due to their exaggerated atomic properties — such as large dipole moments and strong polarizabilities — that can be tuned via state selection [22]. The starting point for neutral atom quantum simulation experiments is cooling, trapping, and detection of individual atoms [23]. These stages have already been developed in our laboratory, as demonstrated in Ref. [24], which reports the first successful trapping of erbium atoms — the atomic species used in our experiment — in optical tweezers. We also discuss the specific properties of erbium and highlight its suitability for Rydberg excitation and laser cooling, which are essential for advancing toward quantum simulation. Finally, we show how to experimentally excite erbium Rydberg atoms, describing the two-photon transition that we use.

## 1.1 Fundamentals of Rydberg atoms

In Rydberg atoms, one of the valence electrons is excited into a state with high principal quantum number $n > 10$. A high principal quantum number, qualitatively implies that there is a valence electron with an orbit far from the nucleus. In this case, the remaining core electrons shield this outer electron from the electric field created by the nucleus. In good approximation — especially for high-l states — the potential is hydrogenic with quantum-defect corrections. The properties of Rydberg atoms therefore closely resemble the ones of hydrogen. The energy of an atom in the state $|n, l, j, m_j\rangle$ is given by:

$$E_{nlj} = -\frac{Ry}{(n - \delta_{lj})^2}, \tag{1.1}$$

where $l$ is the orbital angular momentum quantum number, $j$ the total electronic angular momentum quantum number, $Ry \approx 13.6$ eV the Rydberg constant and $\delta_{lj}$ the quantum defect. The quantum defect arises because, in multi-electron atoms, the inner electron cloud partially shields the nuclear charge. As a result, the potential seen by the valence electron deviates from the pure Coulomb form, leading to corrections in the energy levels.

To work with Rydberg states, it is essential to cool atoms to a temperature close to the absolute zero. The low temperatures are required to confine the atoms within the optical tweezer, which creates a trapping potential on the order of 150 $\mu$K. Furthermore, ultracold conditions are crucial to suppress Doppler broadening of the spectral lines, thereby enabling high-resolution spectroscopy of Rydberg transitions [15].

Using the example of an alkali atom, there is only one valence electron accessible, while the atomic orbitals are fully filled with the remaining electrons. These electrons lead to a shielding of the nucleus, creating a Coulomb-like potential. However, compared to the single proton in a hydrogen atom, the ionic core is much more complex. For alkali atoms with small orbital angular momentum, there is a finite probability for the valence electron to penetrate the cloud of non-valence electrons shielding the core. If this is the case, the shielding is mitigated and the energy level structure changes. Atomic properties, like their dipole moment, their polarizability and their lifetime depend strongly on the principal quantum number $n$ and they are enhanced by working with large values of $n$. Some of these properties are summarized in Table 1.1.

| Property | $n$-scaling |
|---|---|
| Binding energy | $n^{-2}$ |
| Energy between adjacent $n$ states | $n^{-3}$ |
| Orbital radius | $n^2$ |
| Dipole moment $\langle nl\vert er\vert n(l+1)\rangle$ | $n^2$ |
| Polarizability | $n^7$ |
| Radiative lifetime | $n^3$ |

Table 1.1: Scaling of properties of Rydberg atoms with respect to the principal quantum number $n$. Taken from Ref. [22].

For instance, the $n^2$-scaling of the orbital radius leads to the atom size massively increasing for large $n$, reaching values of up to a few microns $(10^4 - 10^5\, a_0)$. Hence, Rydberg atoms are also referred to as "giants" in the atomic world. Another property of Rydberg atoms — making them attractive objects to study — is the long radiative lifetime of the excited state scaling as $n^3$. As a consequence of the large dipole moment scaling as $n^2$, Rydberg atoms are also very sensitive to external electric fields, also including the electric field generated by neighboring Rydberg atoms, with the polarizability scaling as $n^7$. Together with the small spacing between Rydberg levels, scaling as $n^{-3}$, Rydberg atoms are expected to undergo very strong interactions. These strong interactions are governed by two mechanisms: the dipole-dipole interaction and the van der Waals interaction. The former describes the interaction of two dipolar atoms (or molecules), while the latter accounts for interactions of induced dipoles. More precisely, the van der Waals interaction emerges as the fluctuations of the charge distribution of one Rydberg atom give rise to instantaneous dipole moments, which subsequently induce dipole moments in neighboring atoms [22].

## 1.2 Erbium in Rydberg physics

In recent years, advances in the development of scalable quantum platforms have opened new possibilities for the control and manipulation of many-body systems. Among these platforms, neutral atoms trapped in optical tweezer arrays are emerging as powerful tools for quantum simulation, due to their capability to be assembled atom by atom with unprecedented control over both internal and external degrees of freedom [25, 26]. While alkali atoms have so far been the predominant choice for these platforms, their relatively simple electronic structure, characterized by a single valence electron, limits the available tools for control and manipulation. To overcome these limitations, the focus is increasingly shifting toward more complex atoms, such as two-electron atoms (e.g., alkaline-earth and alkaline-earth-like atoms) and lanthanides, including erbium and dysprosium [24, 27].

Erbium, in particular, represents a promising platform for quantum science due to its complex electronic structure, which includes multiple valence electrons and a partially filled $4f$ shell. This complexity provides a broader range of optical transitions, excited states, and magnetic properties compared to alkali atoms, which make erbium ideal for realizing programmable quantum simulators and implementing high-dimensional qudits (d>2), thereby overcoming the limitations of traditional qubit systems [29].

In this context, erbium represents a unique platform for quantum simulations, combining the rich features of lanthanide atoms with the powerful capabilities of Rydberg excitation.

Erbium (Er) is a rare-earth metal and part of the lanthanide (Ln) series. It has an atomic number of $Z = 68$ and a mass of $m = 167.259$ u. As other lanthanides, erbium has a high melting point of 1529°C and a boiling point of 2900°C. There are six different stable isotopes of erbium, and for our experiment we use the bosonic $^{166}Er$, which is the isotope with the highest abundance of 33.6%.

Except for ytterbium, which possesses only filled electronic shells, all Ln elements exhibit an electron vacancy in a highly anisotropic shell ($4f$ for all Ln excluding lanthanum and lutetium) that is surrounded by a fully occupied isotropic

$s$-shell. This special electronic configuration, often referred to as a submerged-shell structure, gives rise to a series of unusual properties that make lanthanides especially interesting for Rydberg experiments. Lanthanides offer the unique possibility to directly couple to $ng$ states with $l = 4$ due to the angular momentum of the submerged shell [30]. Moreover, what makes lanthanide atoms such as erbium particularly interesting, in contrast to alkali atoms, is the possibility to excite electrons from inner $4f$ orbitals. This opens access to a broader range of electronic configurations and excitation pathways, including those involving isolated core-excitation (ICE) of Rydberg states.

### 1.2.1 Electronic configuration

The electronic configuration of the ground state of erbium can be written as:

$$[Xe]4f^{12}6s^2.$$

Here $[Xe]$ corresponds to the electron configuration of xenon.

The occupation of the electrons leads to a submerged shell structure, as the outer $6s$ orbital is filled before the inner $4f$ orbitals are. The $4f$ orbitals are highly anisotropic due to their large angular momentum quantum number of $l = 3$ leading to a strongly anisotropic van der Waals interaction potential. In contrast, the $6s$ orbital with angular momentum quantum number $l = 0$ is spherically symmetric.

The absence of the two electrons out of 14 possible one in the $4f$ orbital, that according to Hund rules have an angular momentum projection number on the chosen quantization axis of $m_l = +2$ and $m_l = +3$ (see Figure 1.1), leads to a large orbital momentum quantum number $L = 5$. The spin projection quantum number of both electrons is $m_s = -1/2$, so the spin quantum number is $S = 1$. The angular momentum quantum number $J = L+S$ (in the standard LS coupling scheme) of the ground state results in $J = 6$. According to the notation $^{2S+1}L_J$ the ground state of erbium can then be written as $^3H_6$.

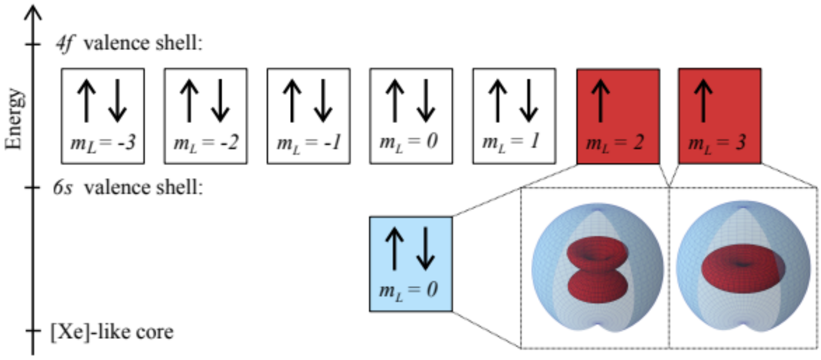

Figure 1.1: Electronic configuration of erbium with emphasis on the partially filled $4f$ shell that gives rise to its characteristic spectroscopic and magnetic properties. Taken from Ref. [31].

### 1.2.2 Relevant erbium transitions

The rich electronic structure of erbium is caused by the submerged-shell structure already mentioned in the previous section. At first, this complexity seems to be disadvantageous for laser cooling and trapping because of unwanted decay channels and spurious excitation possibilities. However, it has been shown that successful laser cooling of erbium atoms is possible, as there are suitable electric-dipole allowed transitions for this purpose [17].

In our experiment the erbium atoms produced in the oven, operated at temperatures of 1100°C and 1200°C, are collimated using transverse cooling (TC) and subsequently slowed down via a Zeeman slower. For these stages, a transition with a broad linewidth ($\Gamma \approx 2\pi \times 30$ MHz) is preferential to ensure many scattering events leading to a strong deceleration force. To be more precise, the strongest transition of erbium near 401 nm is used for the transversal cooling, as well as for the Zeeman slowing process. This transition also allows for ultrafast fluorescence imaging (30 $\mu$s), indeed the broad linewidth gives us a high scattering rate, leading to many scattered photons in a very short time. For this transition one of the $6s$ electrons gets excited into a $6p$ orbital and couples with the remaining $6s$ electron to a $^1P_1$ singlet state. The remaining inner electrons couple via the LS-coupling scheme to a $^3H_6$ state. These two independently coupled systems $J_1J_2$ couple to a $(J_1, J_2)J$ state with electron configuration $[Xe]4f^{12}(^3H_6)6s6p(^1P_1)$.

In contrast, a narrow-line transition near 583 nm is used for the magneto-optical trap, as the small natural linewidth ($\Gamma \approx 2\pi \times 200$ kHz) leads to a lower Doppler temperature and thus to better starting conditions for loading the tweezer traps in later steps of the experiment. This transition is also used for non-destructive imaging. By detuning the imaging laser, we can reduce the scattering rate, which is already small given the narrow linewidth, and preserve the atomic sample with a fidelity of around 96%. This enables us to take one image before the experiment and another after, ensuring that we only analyze data where single atoms are successfully loaded into the optical tweezers. Our single-atom loading scheme, based on light-assisted collisions (LACs), has a 50% probability of loading a single atom in an optical tweezer, and is still based on this transition [32]. In this case, the excited $6p$ electron couples with the $6s$ electron to a $^3P_1$ triplet state. This is a so-called intercombination line as this electric dipole transition violates the spin-conserving selection rule. Analogously to the previously introduced notation, the electron configuration of the resulting state reads $[Xe]4f^{12}(^3H_6)6s6p(^3P_1)$ [33].

An even narrower optical transition ($\Gamma \approx 2\pi \times 8$ kHz) near 841 nm could be employed for sub-Doppler cooling of erbium atoms. As we will discuss later, cooling can play a crucial role in improving the coherence of the Rydberg state, by reducing thermal dephasing and motional broadening effects. In this case one electron of the $4f$ orbital is excited to a $5d$ state. The remaining 11 electrons in the $4f$ shell couple via the standard LS-coupling scheme to form a $^4I_{15/2}$ configuration. The excited state can thus be written as $[Xe]4f^{11}(^4I_{15/2})5d_{5/2}6s^2$.

Finally, our Rydberg state is excited via a two-photon transition at 401 and 411 nm, as will be described in the next section. Here, an atom initially in the $4f^{12}6s^2$ state is excited to the $4f^{12}6sns/nd$ state, i.e. to either the $ns$ or the $nd$ Rydberg series. As a result, approximately 550 different states of the $ns$ and $nd$

Rydberg series with $n$ ranging from 14 up to 140 have been identified [30].

The atomic energy spectrum of erbium for energy values up to $70000\,\mathrm{cm}^{-1}$, with the most important transitions used in our experiment and the corresponding excited states, is shown in Figure 1.2.

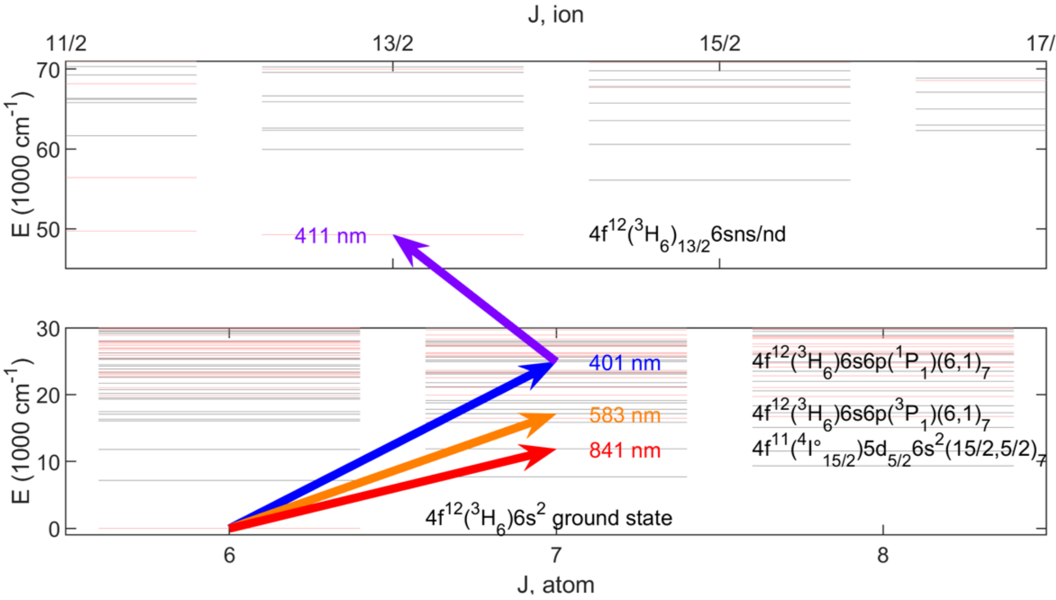

Figure 1.2: Scheme of electronic levels of erbium. The black electronic levels have odd parity, while the red ones have even parity. The arrows indicate dipole-allowed transitions, which can be used for Rydberg excitation via a two-photon excitation scheme. For instance, the 401-411 nm transitions can be used for Rydberg excitation of a $6s$ valence electron.

## 1.3 Excitation Scheme for Rydberg states

Accessing Rydberg states via a single-photon transition is experimentally challenging, especially for high principal quantum numbers $n$, since the corresponding transition wavelengths lie deep in the ultraviolet and become increasingly challenging to reach as $n$ increases. For this reason, we employ a two-photon excitation scheme to drive erbium atoms from the ground state to a Rydberg state.

In our implementation, the excitation proceeds via the absorption of two photons: one at 401 nm and one at 411 nm, as shown in Figure 1.3. By tuning the wavelength of the second photon (around 411 nm) over a range of a few tenths of a nm, we can selectively address different Rydberg series. The intermediate state in this scheme is the $^1P_1$ singlet state, which corresponds to the promotion of a 6$s$ electron to a 6$p$ orbital.

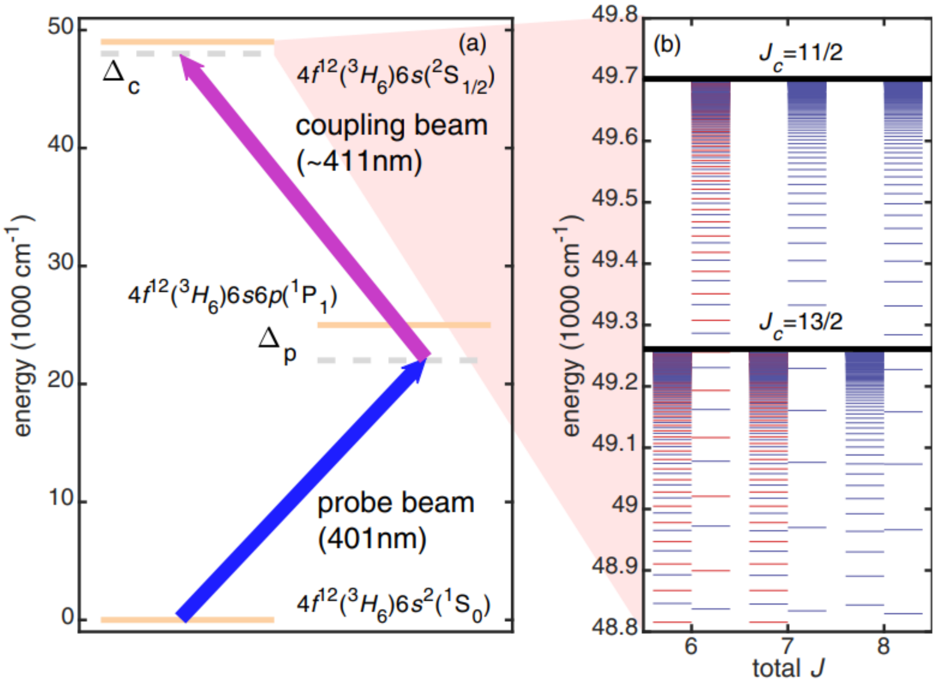

Figure 1.3: Excitation scheme involving the probe transition at about 401 nm with single photon detuning $\Delta_p$ and the coupling transition around 411 nm. Also shown, the two-photon detuning $\Delta_c$. Red (blue) lines indicate the $ns$ ($nd$) series. Taken from Ref. [30].

We define as $|g\rangle$, $|m\rangle$ and $|e\rangle$, respectively the ground, intermediate and excited state. The resonant frequency between ground and intermediate state is $\omega_{mg}$, while between intermediate and excited state is $\omega_{em}$. Thus, we can define $\Delta_p = \omega_p - \omega_{mg}$ and $\Delta_c = \omega_c - \Delta_p - \omega_{em}$ as the detunings of the probe and coupling lasers, respectively. Since our first photon detuning is around 20 $\Gamma$, we can consider $|\Delta_p| \gg \Omega_p, \Omega_c$, so that the intermediate state is adiabatically eliminated. This means that the electrons are effectively excited to the Rydberg state $|e\rangle$ much faster than they would populate the intermediate state, so that $|m\rangle$ remains essentially unpopulated at all times, since the probability of finding an atom in $|m\rangle$ scales as $(\Omega_p/\Delta_p)^2$. In other words, the three-level system can be described as an effective two-level system between $|g\rangle$ and $|e\rangle$.

### 1.3.1 Two-photon transitions

In this section we introduce the theoretical framework of a two-photon transition, under adiabatic elimination approximation. Particular attention is given to the coherence between the ground and excited states. Maintaining coherent oscillations between the ground and Rydberg states is essential for quantum simulation applications, where precise knowledge of the atomic state throughout the entire experiment is required. A complete discussion for two-photon transitions can be found in Ref. [34].

Assuming that the atoms are all initially in the same internal atomic state, and that the intermediate state can be adiabatically eliminated, the effective two-level dynamics is described by the solution of the optical Bloch equations. The population of the excited state $|e\rangle$ evolves as:

$$\rho_e(t) \approx \frac{\Omega_{eff}^2}{\Omega_{eff}^2 + \Delta_{eff}^2} \sin^2\left(\frac{1}{2}\sqrt{\Omega_{eff}^2 + \Delta_{eff}^2}\ t\right), \tag{1.2}$$

where the effective Rabi frequency $\Omega_{eff}$ and the effective detuning $\Delta_{eff}$ are given by:

$$\Omega_{eff} = \frac{\Omega_p \Omega_c}{2\Delta_p}, \quad \Delta_{eff} = \Delta_c + \frac{\Omega_c^2}{4\Delta_p} - \frac{\Omega_p^2}{4\Delta_p}. \tag{1.3}$$

We assume the lifetime of our Rydberg state to be long enough to not cause damping in our Rabi oscillations between ground and Rydberg state. If spontaneous emission from the Rydberg state $|e\rangle$ is included with decay rate $\gamma$, the Rydberg population $\rho_e(t)$ no longer oscillates between 0 and $\frac{\Omega_{eff}^2}{\Omega_{eff}^2+\Delta_{eff}^2}$, but approaches a steady-state value determined by the balance between coherent excitation and decay. For practical applications, it is necessary that the oscillation period between the ground and excited states is shorter than the lifetime of the Rydberg state; this ensures that coherence is preserved and not lost due to spontaneous emission. This requirement justifies our assumption of neglecting spontaneous decay in the present treatment, even if it is not the case for every Rydberg state.

### 1.3.2 Coherence in Rydberg-State Dynamics

A critical requirement in many applications is the ability to maintain coherence between the ground and Rydberg states over extended periods. This coherence is necessary to perform high-fidelity quantum control. Loss of coherence, due to factors such as thermal motion or stray electric fields, as well as spontaneous emission, results in the rapid degradation of the Rabi signal and a transition from a coherent superposition to a statistical mixture. When driving a two-level atom coherently between the ground and a Rydberg state, one observes Rabi oscillations in the population of the excited state. These oscillations are a direct signature of coherent quantum evolution and allow us to deterministically prepare and manipulate the atomic state at any given time.

To achieve a clean Rabi oscillation with the maximum population of the excited state $|e\rangle$ reaching 1, looking at Eq. 1.2, the following conditions must be satisfied.

The maximum population of the excited state is:

$$\rho_e^{\max} = \frac{\Omega_{eff}^2}{\Omega_{eff}^2 + \Delta_{eff}^2}. \tag{1.4}$$

For $\rho_e^{\max} = 1$, the effective detuning must vanish, i.e., $\Delta_{eff} = 0$. The condition $\Delta_{eff} = 0$ implies:

$$\Delta_c = \frac{\Omega_c^2}{4\Delta_p} - \frac{\Omega_p^2}{4\Delta_p}. \tag{1.5}$$

Moreover, the Rabi oscillation frequency is given by:

$$\sqrt{\Omega_{eff}^2 + \Delta_{eff}^2}.$$

To achieve fast and well-defined oscillations, $\Omega_{eff}$ must be sufficiently large, in order to neglect possible oscillations on the effective detuning, that may cause a inhomogeneous broadening of Rabi frequencies, leading to loss of coherence in the oscillation.

A quantum simulation consists in reproducing the dynamics of a target Hamiltonian by means of a controllable physical platform, like Rydberg atoms. For the simulation to be reliable, one must know the precise quantum state of the system at every instant of time. This requirement can only be met if coherence is maintained, since the loss of coherence corresponds directly to the loss of information about the system's state [23].

The coherence of a quantum system is highly sensitive to environmental perturbations, with spontaneous emission being only one of several sources of decoherence. Two other critical factors are thermal motion and DC Stark shifts, both of which degrade the fidelity of Rabi oscillations and limit the coherence time of the system. In order to increase the coherence time of Rydberg excitations in our system, we focus on two main approaches: sub-Doppler cooling, which reduces the residual thermal motion of the atoms, and compensation of stray electric fields in the region where the atoms are excited. Both techniques aim to minimize dephasing and energy level shifts that would otherwise disrupt coherent dynamics.

In the following Chapter, we will present the experimental setup that allows us to perform electric field compensation, but that can also be used for Rydberg atoms detection.

# Chapter 2

# The Experimental Setup

In this Chapter, we describe the experimental setup that I contributed to build during my work in the TREQs laboratory. This setup is designed to perform three tasks: the cancellation of stray electric fields at the center of the vacuum chamber (where our atomic cloud is located); the measure of Stark effect on the Rydberg states; the ionization of the atoms trapped in tweezers. After the ionization of the Rydberg state, the atoms can be detected by two multi-channel plates (MCPs) placed on either side of the chamber. Due to their large dipole moments Rydberg states are extremely sensitive to DC electric fields as we already discussed in Chapter 1 and will explore in more detail in Chapter 3, thus any non-zero static electric fields will quickly disturb spectroscopic measurements of high-$n$ Rydberg states. For this reason, electric field control is crucial for our experiments.

## 2.1 The vacuum chamber

In order to better understand the context in which the electric field control setup is placed, we provide an introduction on the full experimental setup. In Figure 2.1, we show a schematic diagram of our experiment. The tweezers light arrives from the top, being reflected from a dichroic mirror. The fluorescence signal instead, is transmitted from the dichroic mirror and is collected in the corresponding camera, one for each imaging scheme. The imaging beams get into the vacuum chamber from the side viewports.

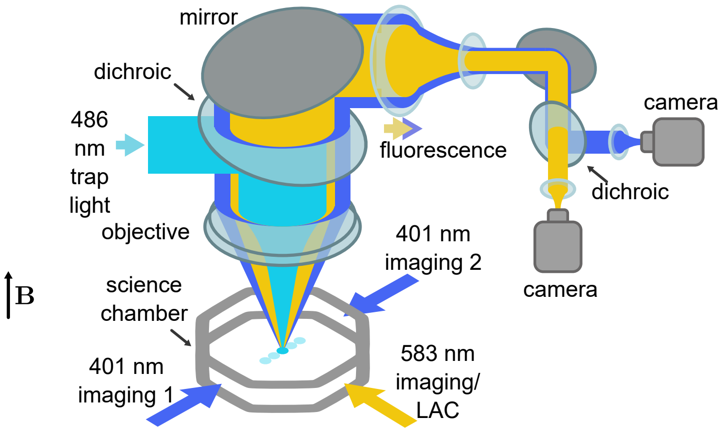

Figure 2.1: Schematic of the science chamber and the optical setup for trapping and imaging. The optical tweezer beam enters the vacuum chamber from the top. The imaging beams are incident from the side, and the resulting fluorescence is collected by two cameras placed above the chamber. A dichroic mirror separates the optical paths of the tweezer light and the fluorescence.

Two large viewports at the top and bottom and five side viewports on the octagonal chamber provide optical access to the experiment.

The small viewports are coated with a broadband antireflective magnesium-fluoride coating. In the range from 380 nm to 450 nm, where further Rydberg excitation steps may be implemented, the reflectivity $r < 1.5\%$.

## 2.2 The Electric Field Plates

Electric field control inside the vacuum chamber is enabled by a set of electrodes or field plates placed inside the vacuum chamber, as shown in Figure 2.2. Eight field plates in two groups are used, one situated above and one below the atom cloud. Each group of four is arranged in a fourfold-symmetric geometry resembling a clover-leaf pattern, as can be seen in Figure 2.3. This arrangement is suited to

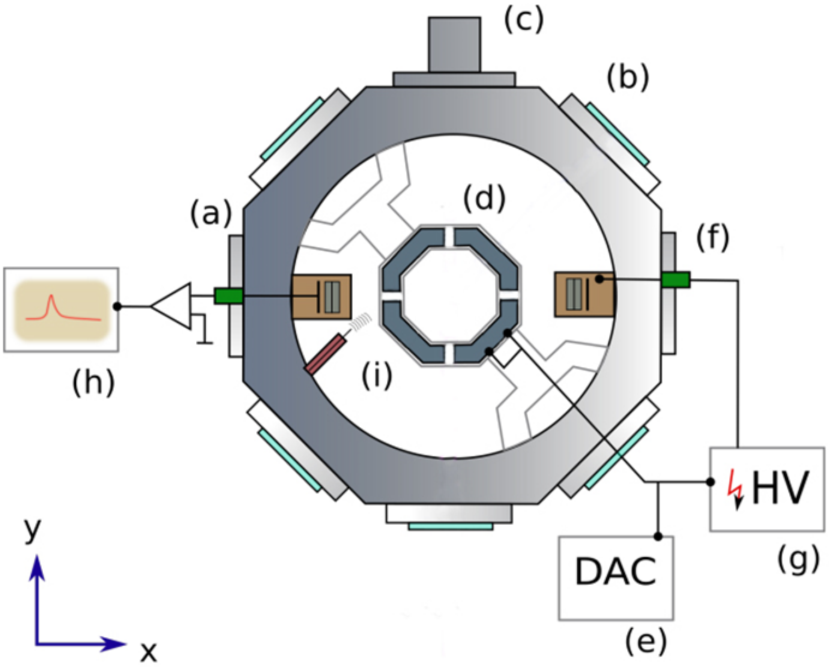

Figure 2.2: The components of the Rydberg chamber. (a) The vacuum chamber. (b) Viewports coated for our specifc wavelengths. (c) Connection to main chamber. (d) Field plates. (e) Low voltage control of the field plates. (f) MCP detectors and voltage feedthroughs. (g) High voltage supply for the MCPs and field plates. (h) Amplifier for the MCP signal. (i) Feedthrough for microwave fields.

generate arbitrary electric field vectors at the atom cloud with a good spatial homogeneity.

We can use the transformation matrix in Table 2.1 to determine the voltage to apply to each electrode in order to generate a desired electric field in any direction.

For instance, if we want to generate an electric field **F** along the $x$-axis, we can set $D_x = 1$ V. To convert the voltage $D_x$ to an electric field applied on the atoms, we used the simulation software COMSOL, defining our actual setup.

At present, the field plates serve two main purposes: compensation of stray electric fields and ionization of Rydberg atoms. By ionizing the Rydberg atoms before imaging, we prevent them from decaying back to the ground state and this

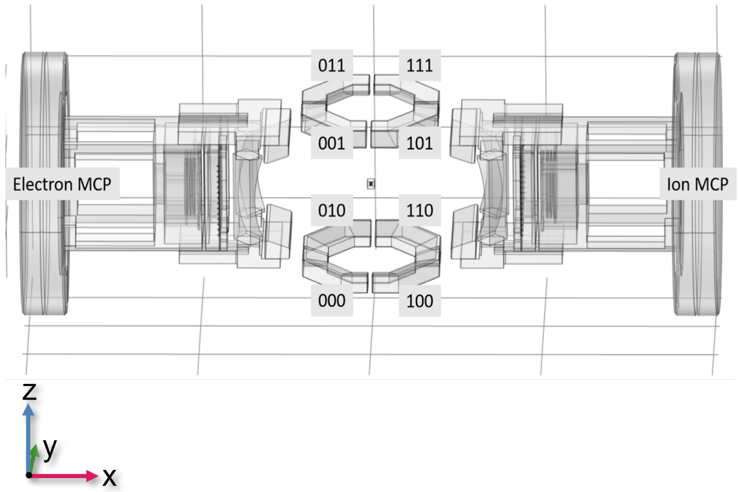

Figure 2.3: COMSOL representation of the inside of the vacuum chamber. The eight electrodes are labeled using a binary numbering scheme. The two MCPs are placed in opposite sides of the vacuum chamber.

$$\begin{pmatrix} U_{000} \\ U_{100} \\ U_{010} \\ U_{110} \\ U_{001} \\ U_{101} \\ U_{011} \\ U_{111} \end{pmatrix} = \begin{pmatrix} 1 & 1 & 1 \\ -1 & 1 & 1 \\ 1 & -1 & 1 \\ -1 & -1 & 1 \\ 1 & 1 & -1 \\ -1 & 1 & -1 \\ 1 & -1 & -1 \\ -1 & -1 & -1 \end{pmatrix} \begin{pmatrix} D_x \\ D_y \\ D_z \end{pmatrix}$$

Table 2.1: Transformation matrix used to determine the voltages to apply on each electrode in order to generate a desired electric field along a specified direction.

allows us to detect the excitation of atoms via ground state loss in fluorescence imaging. Indeed, ground-state atoms can't be ionized, even applying the maximum electric field of 653.58 V/cm, that corresponds to applying -3 kV on the electrodes 111, 101, 110 and 100 and 3 kV on 011, 001, 010 and 000.

Neglecting the Stark shift, and expressing the binding energy in terms of $n$, we obtain the result for the classical field for ionization [15]

$$F = \frac{5.14 \times 10^9}{16n^4}\ \mathrm{V/cm}. \tag{2.1}$$

This relation allows us to estimate the electric field required to ionize a given Rydberg state and to identify the Rydberg states that can be ionized with our setup. The results are shown in Figure 2.4.

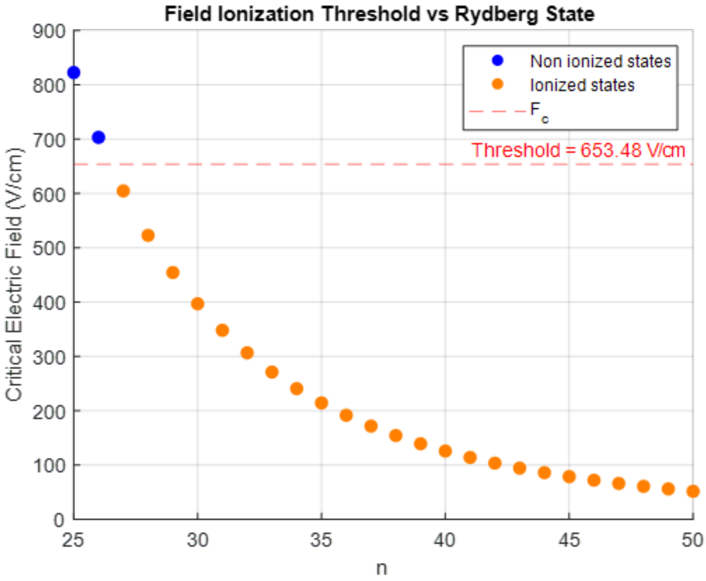

Figure 2.4: Electric field required for ionization as a function of the principal quantum number $n$ of the Rydberg state. The dashed red line indicates the maximum electric field achievable with our setup (±3 kV applied to the electrodes). In this way, we can ionize atoms with $n \geq 27$.

The field plates could also be used for measuring Stark maps of different states applying low voltages, and for Rydberg states detection using the MCPs.

On closer inspection, these tasks place high demands on the voltage supply, which needs to provide voltages over a range of magnitudes (for ionization) with high stability (for electric field compensation). To meet these requirements, the system is designed with two separate voltage sources and a high-speed switch to select one of them. The precise voltage sources are 16 bit DACs and can supply from -10 V to 10 V with a precision of 0.3 mV. The high-voltage sources supply up to 3 kV.

The ionization field is mediated by the same field plates that also perform the electric field control in the chamber. Ionization corresponds to generating an electric field vector of a much higher field strength than can be provided by the field control. Therefore, the field plates can be switched to a high voltage on demand to generate the ionization field. To perform Rydberg states detection with the MCPs, an electrostatic lens system needs to be ramped up at the same time, to push the ionic and electrons beams toward the MCPs. A pair of wire grids, one before each MCP, are placed to shield the electric field generated by the high voltage applied on the MCP. This is required to generate secondary emission electrons, as will be discussed in the next section.

## 2.3 Multi-channel plates

As already mentioned, the setup can allow us to detect Rydberg atoms exploiting their susceptibility to ionization. After the ionization field is applied by the electrodes, ions and electrons are accelerated along the field lines in opposite direction. Two MCP detectors are built into the chamber in order to detect these fragments with high efficiency. The working principle of an MCP is much the same as that of a photo-multiplier tube. It consists of millions of ultrathin conductive glass capillaries from 4 $\mu$m to 25 $\mu$m in diameter and 0.2 mm to 1.0 mm in length. They are fused together and sliced in the shape of a thin plate. Each one of these capillaries functions as an independent secondary electron multiplier if there is an electric potential difference of several kV between the front and the back of the plate. Indeed, after each scattering event, the electrons must acquire new kinetic energy from the electric field through the voltage gradient, to generate a cascade of secondary emission electrons.

The MCPs used are the F4655-10S184 by Hamamatsu. They are two stage

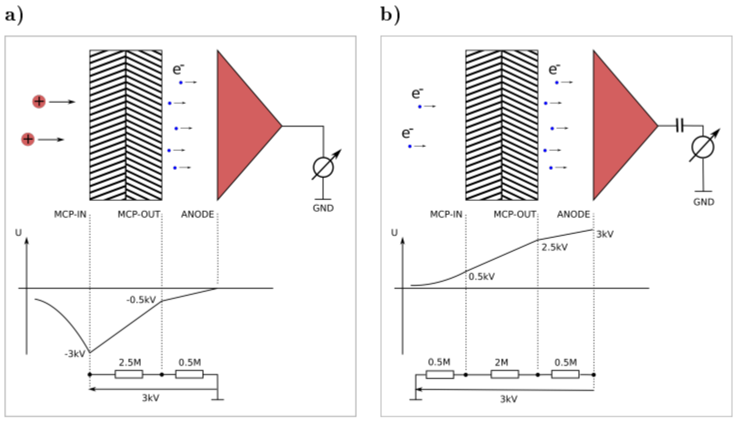

Figure 2.5: Principle of operation and connection diagram of the MCPs. The two hatched rectangles are two stacked multi-channel plates of a 2-stage MCP assembly. The red triangle is the detector anode collecting the electrons multiplied by the MCP. a) Detection of positive ions requires a negative potential at MCP-IN. Starting at rest at zero potential, the ions acquire a kinetic energy of 3 keV. b) Detection of electrons requires a positive potential at MCP-IN. Because an avalanche of electrons is triggered on impact, the electric potential must rise from MCP-IN to MCP-OUT to ANODE, regardless of detection mode. Therefore, a large potential at the ANODE in b) is unavoidable.

MCP assemblies, meaning that two MCPs are stacked face to face to increase the gain. The typical gain of this type is $10^7$ at 3 kV supply voltage. The production of secondary emission electrons is limited by the dead time of the channels, due to the temporary depletion of electrons within the channel walls after an avalanche event. The gain starts to saturate at an output current of about 0.1 $\mu$A. This means that it is not possible to reach higher output currents because the electrons within the MCP channels are temporarily depleted. Even without any ion impact, the MCP will show a low dark current of 1.5 pA.

The electron detection efficiency for electrons with 500 keV kinetic energy, corresponding to 500 V on the electrons MCP-IN, is at 85% and the ion detection efficiency for kinetic energies above 2 keV (we have -3 kV on the ions MCP-IN) is reported to be greater than 60%. These values are taken from the MCPs manual.

The recommended supply voltage at each one of the three MCP connections is shown in Figure 2.5. The electric potential must rise from MCP-IN to MCP-OUT to ANODE, regardless of detection mode, in order to accelerate the charges once they reach the MCP-IN part of the detector. A capacitor is placed in series with the the voltmeter (which is basically a resistance) for the electrons detection and not for the ion one. This is basically because we want an AC filter to block the DC voltage set on the anode (3 kV) letting pass only the AC voltage generated by the electrons. In the ions case, instead, the anode is grounded and so there is no DC voltage that requires to be filtered.

The electrons reaching the anode of each MCP generate a current, corresponding to a flow of charged particles. This current is then converted into a voltage, according to Ohm's law, which can be directly measured on an oscilloscope.

In front of each MCP there is a wire grid that allows ions and electrons to pass through but also shield the electric field generated from the MCP potential. Moreover, a lens composed of four electrodes is placed in front of the wire grid and will be active only when the ionization pulse is on, in order to focus the charged fragments into the MCPs.

## 2.4 Electronic Control Systems

All of the components described above are going to be controlled using the dedicated rack that I built, following the connection scheme sketched in Figure 2.6.

In the following, we describe the components used in the low- and high-voltage regimes.

### 2.4.1 Low-Voltage range

The low-voltage range includes one voltage source for each of the eight field plates (8x 16 bit DACs channels), eight voltage sources (8x 16 bit DACs channels) for the electrodes that compose the lens system and two sources (2x 18 bit DACs channels) for the wire grids.

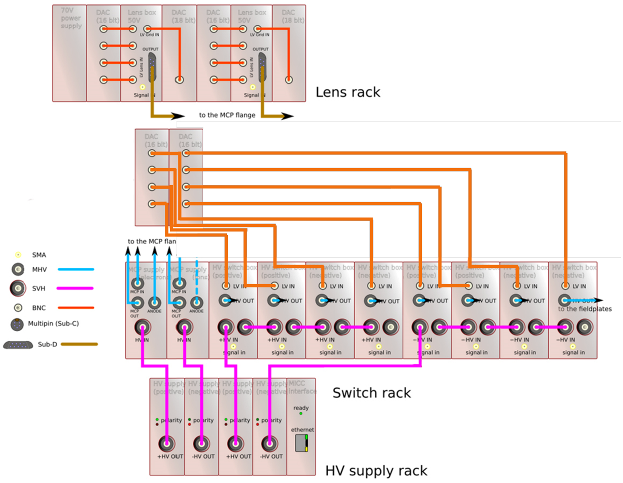

Figure 2.6: Electronic setup for low- and high-voltage. The Lens Rack supplies the lens system and the wire grid in front of each MCP detector. It draws its supply voltage respectively from 16- and 18-bit DACs, which are supplied by BK Precision 9174B voltage supplier. The Field plate Rack consists of eight 16-bit DACs to supply the field plates during electric field compensation. The eight field plate voltages are passed into the Switch Rack, where they can be switched from low- to high-voltage during ionization. The HV Supply Rack is a modular high-voltage source are ISEG HV DPR 30 405. The MCPs supply is further split up in a high-voltage divider, according to the MCPs section.

All eight field plates contribute to the electric field compensation during normal operation. When the ionization pulse is applied, they are switched to high voltage. Their voltage sources are therefore connected to the high-voltage switches, that choose either high- or low-voltage. In case we want to use the MCPs for Rydberg detection, the switches in the lens rack receive the signal to charge up the electrostatic lens systems in front of each detector, simultaneously with the switching of the electrodes from LV to HV. Meanwhile, the shielding grid in front of each detector is continuously supplied by its own low-voltage source. The voltage supplies for the field plates as well as for the shielding grids need to be highly stabilized. All fluctuations in their output voltage directly affect the electrostatic environment we aim to keep as stable as possible.

### 2.4.2 High-Voltage range

The high voltage part comprises the supply for the MCP detectors and the high voltage source to charge up the field plates for the ionization of Rydberg atoms. Both the detectors and the field plates are supplied with up to 3 kV, which enable the detection of Rydberg levels as low as $n = 27$, as shown before. For this reason, both are supplied by a single modular power supply with four independent output channels, each of which can provide positive or negative voltage on demand.

Two channels are used for the MCP supply and two for HV switches as illustrated in Figure 2.6. Each output channel is a DPR 30 405 power supply module in the 3U MMC version built by ISEG. They are bundled together in one MMC crate, that supplies all channels with a stable powerline input voltage and handles the set points for each output voltage. The output voltages of each channel are controlled via the USB-port. On the control computer, the status and set-points of each channel can be controlled by the software isegSCPIControl. Besides the nominal voltage of 3 kV, the fluctuations and the resolution of the voltage source is of interest. The chosen voltage source features a ripple and noise of $< 3$ mVpp (typically) and 7 mVpp (max). The output voltage is set by a digital-analog-converter (DAC) with 20 bits resolution by the MMC crate. The incremental step size is therefore $2^{-20} \approx 1$ ppm and the voltage can be set in steps of 3 kV Œ 1 ppm = 3 mV. Our tests revealed that the actual voltage applied is always around 4 V smaller the set one, and this is also shown by the control software.

From the point of view of the MCP detectors, a stable voltage is necessary to guarantee a constant signal per count. Because of the operating principle of MCPs, a small fluctuation in the supply voltage between the plates causes a significantly smaller or larger avalanche of electrons and thus a great change in the output signal per incident particle. From the gain characteristics curve in the specification sheet of the MCP detectors, the impact can be estimated. The relative change in gain is approximately $10^{-6}$ for a fluctuation of 7 mVpp, which is the maximum fluctuation of our voltage source. The voltage supply should therefore not present a source of error in the output signal. From the point of view of the field plates, any fluctuations in the ionization voltage affects the desirable state-selective ionization capability and the highest Rydberg state, that can be selectively ionized. In this setup, the ripple voltage of 7 mVpp corresponds to the difference in ionization voltage between Rydberg states $n = 240$ and $n = 241$. These represent the highest Rydberg states that can be distinguished in principle. These considerations show that the high-voltage sources should not present a limit to the detection capabilities.

The electronic circuitry and characterization of all of these components is described in Appendix A.

# Chapter 3

# DC Stark shift compensation

Rydberg atoms are extremely sensitive to external electric fields due to their large polarizabilities and spatially extended wavefunctions. The strong dependence of the polarizability on the principal quantum number ($\alpha \sim n^7$) results in DC Stark shifts which can be substantial in our system.

Although this high sensitivity is advantageous for field sensing applications [35], it also makes Rydberg systems particularly susceptible to decoherence due to stray electric fields. As explained in Chapter 1, it is crucial to minimize decoherence to realize effective Rydberg-atom-based quantum simulators.

For this purpose, we have used the setup described in Chapter 2, in order to implement a compensation scheme that reduces the electric field experienced by the atoms. Finally, I present the measurements I have carried out as first steps towards the final compensation arrangement.

## 3.1 The DC Stark Shift

A crucial source of decoherence arises from DC Stark shifts caused by stray electric fields in the laboratory environment. For instance, stray electric fields may appear because of surface charges on viewports and isolated components of the science chamber. In hydrogen-like atomic systems, composed of a single electron bound to a positively charged ion, such as highly excited Rydberg atoms, the interaction with an external electric field leads to a modification of the atomic energy levels. This phenomenon is known as the Stark effect [36].

The Stark effect can be linear due to permanent or induced dipole moments of the atoms. However, in the case of hydrogen-like systems, and particularly in spherically symmetric states with no permanent dipole moment, the first-order Stark effect vanishes. As a result, the dominant contribution to the energy shift arises from second-order perturbation theory, resulting in the quadratic Stark effect. The energy shift due to the quadratic Stark effect is given by

$$\Delta E = -\frac{1}{2}\alpha F^2, \tag{3.1}$$

where $\alpha$ is the static electric polarizability of the state and $F$ is the magnitude of the applied electric field.

As shown in Table 1.1, the polarizability of Rydberg atoms scales as $n^7$, therefore the dependency of the quadratic Stark shift on the principal quantum number and on the electric field will be:

$$\Delta E \sim -\frac{1}{2}n^7 F^2. \tag{3.2}$$

This shift effectively changes the resonance frequency altering the effective detuning as:

$$\Delta'_{eff} = \Delta_{eff} - \frac{\Delta E}{h} = \Delta_{eff} + \frac{\alpha F^2}{2h}. \tag{3.3}$$

If we now consider the uncorrelated fluctuations of the new effective detuning, we obtain

$$\sigma_{\Delta'_{eff}} = \sqrt{\sigma^2_{\Delta_{eff}}\left(\frac{\partial \Delta'_{eff}}{\partial \Delta_{eff}}\right)^2 + \sigma^2_F\left(\frac{\partial \Delta'_{eff}}{\partial F}\right)^2} \quad \approx \quad \sigma_F\frac{\alpha F}{h}, \tag{3.4}$$

where we neglect the fluctuations on the effective detuning $\sigma_{\Delta_{eff}}$ since our lasers are frequency-locked. This result shows that the detuning fluctuations depend linearly on the electric field. As we can notice from Eq. 1.2, strong fluctuations of the detuning induce fluctuations in the oscillation frequency of the system, ultimately leading to decoherence. To reduce this kind of contribution to our detuning uncertainty, we need to minimize the total electric field applied to our atoms. An intuitive understanding of this behavior is illustrated in Figure 3.1.

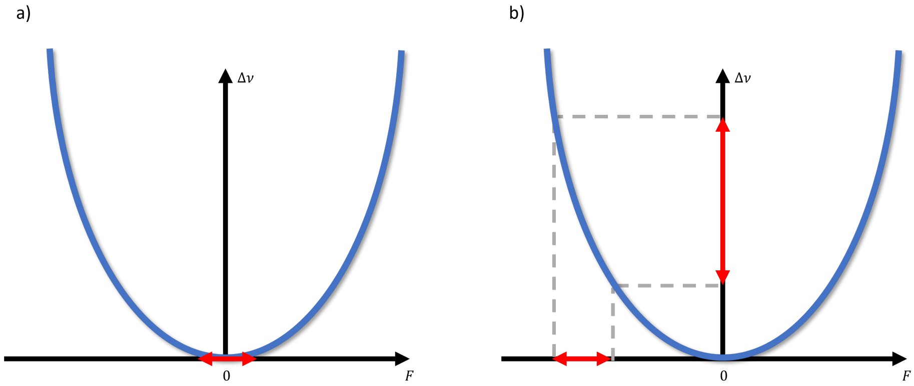

Figure 3.1: Effect of electric field fluctuations on the resonance frequency. For the same amplitude of electric field fluctuations, the resulting fluctuation in frequency Stark shift is small at low electric fields (a) and large at high electric fields (b).

The Stark-induced energy shift $\Delta E$ can also be used to determine the static polarizability $\alpha$ of the Rydberg state. By measuring the energy shift $\Delta E$ or the corresponding frequency shift $\Delta\nu$ (where $\Delta\nu = \Delta E/h$), one can directly extract the value of $\alpha$.

In a more complete description, the Stark shift can be expressed as [34]:

$$\Delta E_{|J,m_J\rangle} = -\frac{1}{2}\alpha^{(0)}(J)F^2 - \frac{1}{4}\alpha^{(2)}(J)\left(3F_z^2 - F^2\right)\left[\frac{3m_J^2 - J(J+1)}{J(2J-1)}\right], \qquad (3.5)$$

where $\alpha^{(0)}(J)$ is the scalar polarizability and $\alpha^{(2)}(J)$ is the tensor polarizability. $F_z$ is the component of the electric field along the quantization axis, which is fixed by the magnetic field. In the case of $47s$ state: $J = 6$ and $m_J = -6$.

This formula allows us to determine the polarizability components $\alpha^{(0)}(J)$ and $\alpha^{(2)}(J)$ from experimental measurements. The scalar polarizability $\alpha^{(0)}(J)$ represents the isotropic response of the system to the electric field, while the tensor polarizability $\alpha^{(2)}(J)$ accounts for the anisotropic contribution, which depends on the orientation of the electric field relative to the quantization axis. In this case, we assume that the Stark shift of the ground state is negligible compared to the Stark shift of the Rydberg state. This assumption is well justified, given that the Stark shift of the Rydberg state scales as $n^7$. Therefore, Eq. 3.5, which describes the Stark shift of the Rydberg state, represents in good approximation the total shift of the transition frequency.

## 3.2 Experimental implementation and results

In our measurements the quantization axis, defined by the magnetic field **B**, lies in the xy plane, and it is aligned to the direction of the two Rydberg excitation laser beams. Both Rydberg beams are left-handed circularly polarized and counter-propagating. In this configuration, only the $\sigma^-\sigma^+$ transition is addressed: because the magnetic field is oriented opposite to the propagation direction of the 411 nm beam, the atoms effectively perceive its polarization as right-handed. Figure 3.2 shows a schematic picture of the magnetic field orientation.

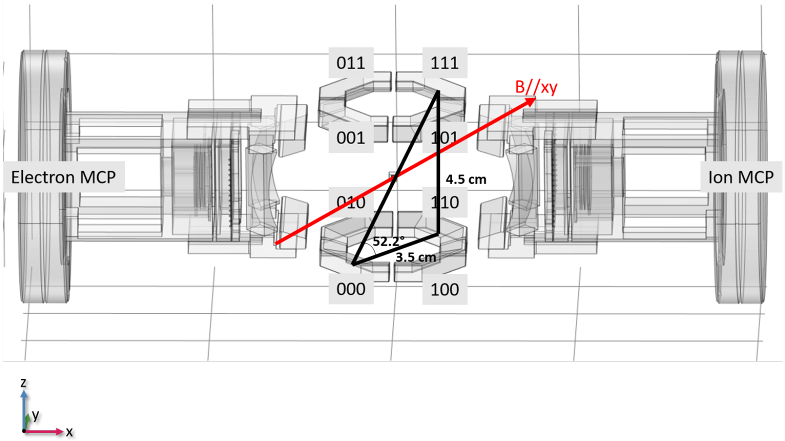

Figure 3.2: Orientation of the magnetic field **B** defining the quantization axis. The field lies in the $xy$ plane, aligned with the direction of the Rydberg excitation laser beams.

As a first approach to stray electric field compensation we initially used only a pair of opposite electrodes as shown in Figure 3.3. Compensate with all eight electrodes would give us the possibility to compensate for any field direction, but it would also increase the complexity of our setup.

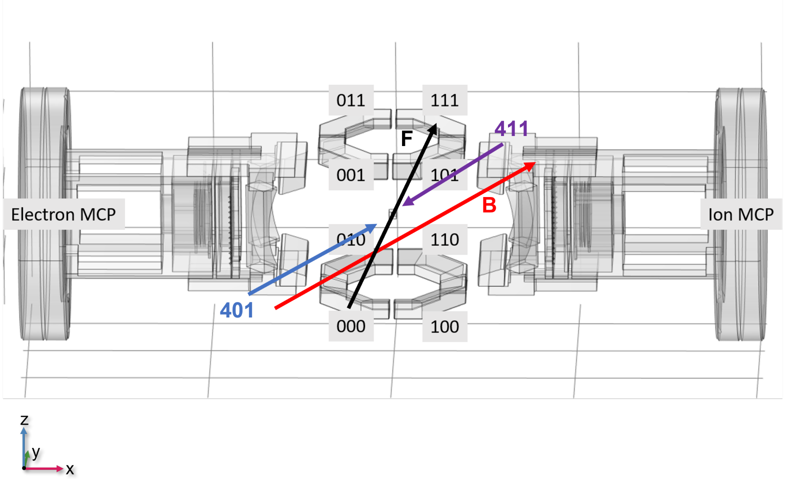

Figure 3.3: Configuration of the electric field used to compensate for stray electric fields in the vacuum chamber. The electric field **F** is applied using the electrodes 000 and 111, scanning different voltages.

In this configuration, the electric field vector has a component aligned to the magnetic field set during the Rydberg excitation, which means $F_z \neq 0$ in Eq. 3.5. Indeed, the angle between the quantization field $B$, which defines the $z$-axis, and the electric field $F$ is 52.2°. This implies that the $z$-component of the electric field is given by:

$$F_z = \cos(52.2°) \cdot F = 0.61 \cdot F. \tag{3.6}$$

To understand the geometry of the system, we consider the distances between the electrodes and the center of the chamber. The distance from the center to each electrode is calculated as:

$$\frac{\sqrt{3.5^2 + 4.5^2}}{2} = 2.85\,\mathrm{cm}. \tag{3.7}$$

In the previous equation 3.5 cm is the distance between electrode 000 and electrode 110 and 4.5 cm is the distance between electrode 110 and electrode 111 (see Figure 3.2). These dimensions, which represent the height and length of the electrodes setup, were obtained from a SolidWorks model of the electrodes, since access to the vacuum chamber for a direct measure is not possible. As a consequence, it is also difficult to estimate the uncertainty on these values. This distance is useful to convert the voltage applied on each electrode to an electric field applied on the atoms, for the simple case of two electrodes, using the formula:

$$F = V/d, \tag{3.8}$$

since the voltage is nearly uniform over this distance. Here $V$ is the voltage difference applied between the two electrodes and $d$ is the distance separating them.

Using the Pythagorean theorem, we calculate the diagonal of the system as:

$$d = \sqrt{3.5^2 + 4.5^2} = 5.7\,\text{cm}. \tag{3.9}$$

To determine the angle $x$ between the diagonal and the horizontal axis, we use the relationship:

$$5.7 \cdot \cos(x) = 3.5. \tag{3.10}$$

From this, we find that:

$$x = 52.2^\circ, \quad \text{and indeed } \cos(52.2^\circ) = 0.61. \tag{3.11}$$

This confirms the orientation of the electric field relative to the quantization axis.

We performed spectroscopy measurements of the $47s$ state of erbium while varying the electric field applied to the atoms. For this purpose, we loaded single atoms into a 5×1 optical tweezer array aligned along the Rydberg excitation beams. Using five tweezers allows us to collect more data for every experimental execution, thus shortening the overall experiment time. After single-atom loading, we apply different values of electric field along the direction of the two electrodes and then we apply a 25 $\mu$s Rydberg excitation pulse, scanning different frequencies of the first photon, while the tweezers were turned off to avoid AC

Stark shifts of the resonance. Immediately after the excitation, the same two electrodes were switched to +700 V and -700 V respectively for 5 $\mu$s , to ionize the excited Rydberg atoms and prevent them from decaying back to the ground state before being imaged at 401 nm. The Stark shift measured in this case is shown in Figure 3.4.

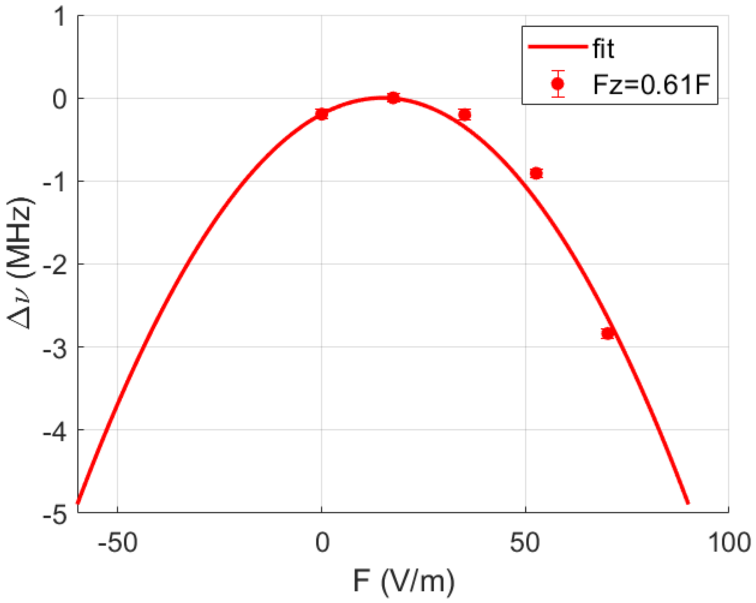

Figure 3.4: Measured Stark shift as a function of the applied electric field for $F_z = 0.61 \cdot F$. The data shows a parabolic dependence, as expected from the quadratic Stark effect.

The maximum of the parabola is observed for an electric field of around 14 V/m, which corresponds to a voltage of 0.4 V applied to electrode 000 and -0.4 V applied to electrode 111. In this case, the Stark shift results in a decrease in the transition frequency, as shown in Figure 3.5.

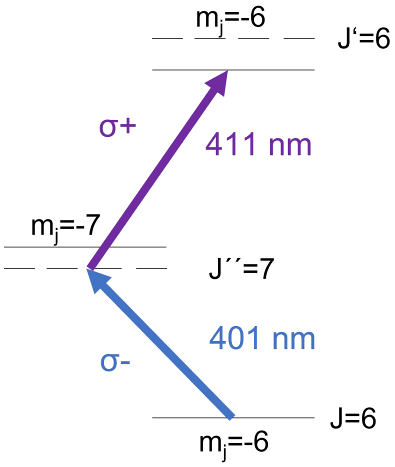

Figure 3.5: Transition frequency shift measured for $F_z = 0.61 \cdot F$. The shift corresponds to a reduction in the transition frequency due to the applied electric field.

After this first step, we tested a second pair of electrodes to compensate for stray electric fields along a different direction. Performing two different measurements for different values of $F_z$ was useful to confirm the direction dependence of the Stark shift and also to calculate the static polarizability of the Rydberg state. The configuration of the electrodes for this second case is shown in Figure 3.6. In this case $F_z = 0$, since the electric field is perpendicular to the quantization axis.

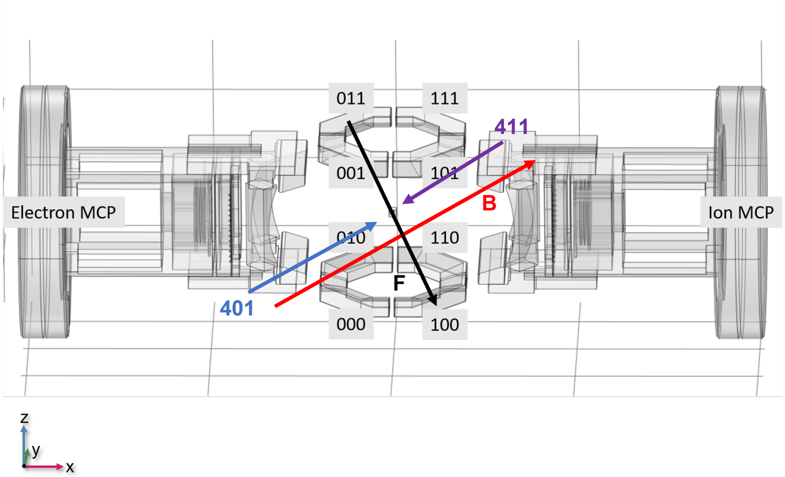

Figure 3.6: Configuration of the electric field used to compensate for stray electric fields in the vacuum chamber. The electric field **F** is applied using the electrodes 011 and 100, scanning different voltages.

The Stark shift measured in this configuration is shown in Figure 3.7.

The Stark shift was minimized for an applied electric field of 10.5 V/m that corresponds to 0.3 V set on 100 electrode and -0.3 V on 011. The Stark shift is towards higher frequencies, due to the different sign of the polarizability tensor along this direction, as shown in Figure 3.8.

Finally, we tested whether applying electric field compensation could improve the Rabi oscillations between the ground and the Rydberg state. Using a similar protocol than the one that we used for the spectroscopy, we performed a Rabi oscillation measurement. In this case we fixed the voltages on the two electrodes in order to minimize the electric field experienced by the atoms. Moreover, we fixed the first photon frequency in order to be resonant with the Rydberg transition, but scanning different durations of the Rydberg excitation pulse, as shown in Figure 3.9.

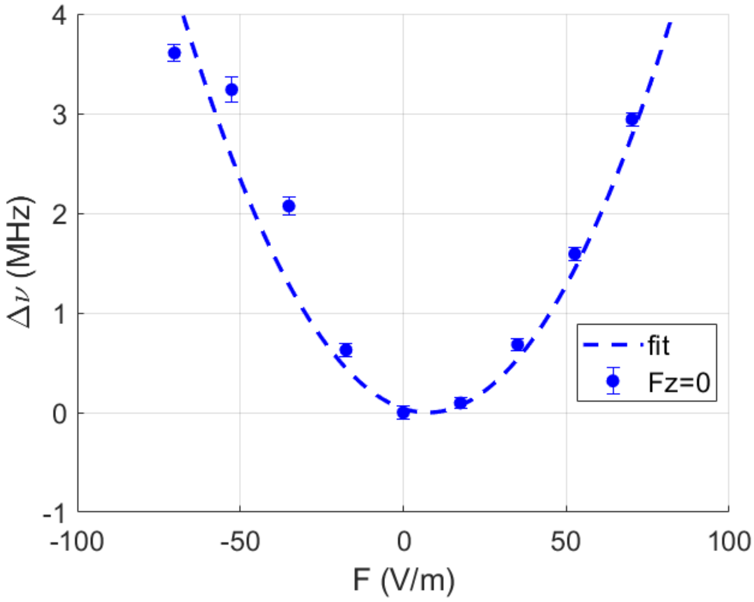

Figure 3.7: Measured Stark shift as a function of the applied electric field for $F_z = 0$. The data shows a parabolic dependence, as expected from the quadratic Stark effect.

Indeed, the Rydberg atoms population gets bigger if we apply a field compensation, but no improvement in the damping of the oscillation seems to appear. We found out that this problem is due to the short lifetime of our $47s$ Rydberg state, which is around 2 $\mu$s.

The next step of these measurement would be to repeat it compensating independently along the x, y and z axis. We can set the electric field to the minimum value determined from the measurement, and use this configuration for all subsequent Rydberg measurements. This compensation measurement should be repeated daily, or at least before each important measurement, since electric field drifts caused by charged particles in the vacuum chamber can be neglected over the course of hours, but not over days [37]. Anyway, this compensation would only be effective for states with a longer lifetime, otherwise spontaneous emission would reduce our Rydberg population after a single oscillation.

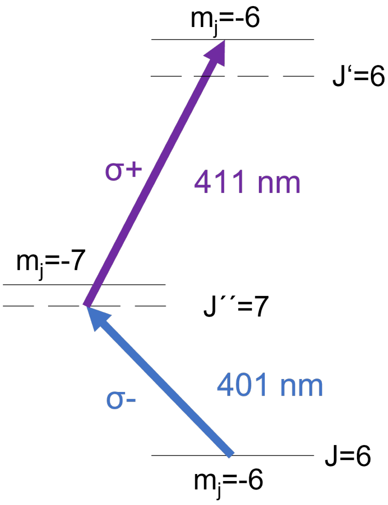

Figure 3.8: Transition frequency shift measured for $F_z = 0$. The shift corresponds to an increase in the transition frequency due to the applied electric field.

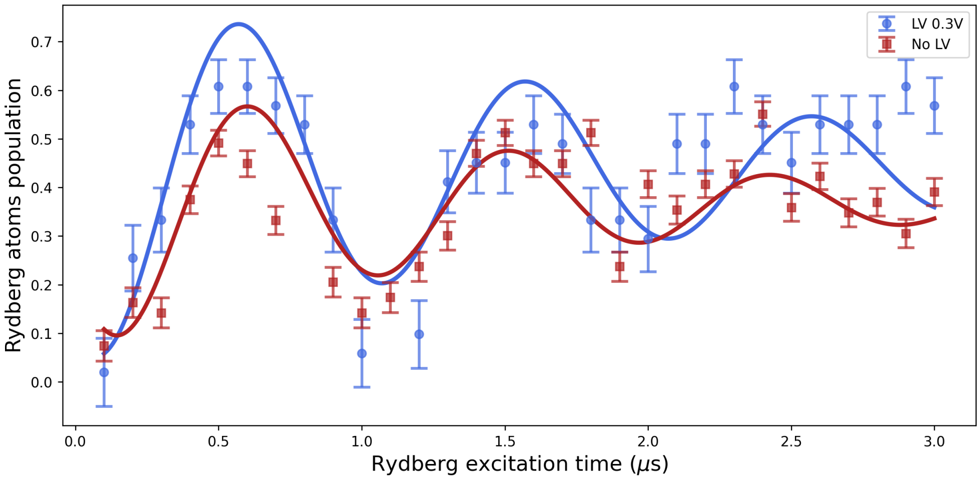

Figure 3.9: Rabi oscillations observed with (blue dots) and without (red squares) low-voltage compensation applied to minimize stray electric fields. The fits are performed considering a sinusoidal behavior multiplied by an exponential damping.

## 3.3 47s Rydberg state static polarizability

As already discussed, Rydberg atoms are very sensitive to electric fields, as a consequence the Stark shift of Rydberg states is big and their polarizability is big as well and can be calculated starting from Stark shift measurements.

We investigated the DC Stark shift of the $47s$ Rydberg state in erbium by applying electric fields using different electrodes configurations. As described in the previous section, we observed that changing the direction of the electric field (by applying voltages to different pairs of electrodes) caused a reversal in the sign of the Stark shift. Specifically, the Stark shift for the same state showed opposite curvature in the two configurations. This directional dependence of the Stark shift, indicates that the polarizability is not purely scalar. In general, the polarizability $\alpha$ of an atomic state can be decomposed into a scalar and a tensorial contribution, as we can see from Eq. 3.5.

In practice, the applied field induces a shift in both the Rydberg state and the ground state, and what we measure experimentally is the variation of the transition frequency.

We started by fitting the two coupled parabolas modeled by:

$$\begin{aligned}\Delta\nu_1 &= \frac{1}{h}\left[-0.5\cdot\alpha_0 - 0.25\cdot\alpha_2\cdot(3F_z^2 - F^2)\right]\cdot F^2\\ &= \frac{1}{h}\left[-0.5\cdot\alpha_0 - 0.25\cdot\alpha_2\cdot 0.1163\right]\cdot F^2,\\ \Delta\nu_2 &= \frac{1}{h}\left[-0.5\cdot\alpha_0 + 0.25\cdot\alpha_2\right]\cdot F^2.\end{aligned}$$

as shown in Figure 3.4 and Figure 3.7.

From the fits, we obtained:

$$\begin{aligned}\alpha_0/h &= (1.41\pm0.14)\times10^6\,\mathrm{Hz}\cdot\left(\frac{\mathrm{cm}}{\mathrm{V}}\right)^2,\\ \alpha_2/h &= (5.65\pm0.31)\times10^6\,\mathrm{Hz}\cdot\left(\frac{\mathrm{cm}}{\mathrm{V}}\right)^2.\end{aligned}$$

Comparing Eq. 3.1 and 3.5, we notice that the total polarizability can be written as:

$$\frac{\alpha(\theta_p)_{J,m_J}}{h} = \alpha_0 + \frac{1}{2}\alpha_2\big(3\cos^2(\theta_p) - 1\big)\left[\frac{3m_J^2 - J(J+1)}{J(2J-1)}\right] \tag{3.12}$$

In the two cases we measured, for $\theta_p = 52.2°$ and $\theta_p = 0$, we get a total polarizability of:

$$\frac{\alpha(52.2°)_{6,-6}}{h} = \frac{\alpha_0}{h} + \frac{\alpha_2}{2h}\big(3\cos^2(52.2°) - 1\big) = (1.76 \pm 0.14) \times 10^6\,\mathrm{Hz} \cdot \left(\frac{\mathrm{cm}}{\mathrm{V}}\right)^2, \tag{3.13}$$

$$\frac{\alpha(0°)_{6,-6}}{h} = \frac{\alpha_0}{h} + \frac{\alpha_2}{2h}\big(3\cos^2(0°) - 1\big) = (7.12 \pm 0.34) \times 10^6\,\mathrm{Hz} \cdot \left(\frac{\mathrm{cm}}{\mathrm{V}}\right)^2. \tag{3.14}$$

In particular, we can compare our values to the Rydberg state $45s$ of rubidium, which is $\alpha_0/h = 2.49 \times 10^7\,\mathrm{Hz} \cdot \left(\frac{\mathrm{cm}}{\mathrm{V}}\right)^2$ [38]. In the case of an $s$ state of rubidium the tensorial contribution of the Stark shift is zero, since $F$ =1/2 and $m_F = \pm 1/2$. The values that we got for different directions of the electric field, are one order of magnitude smaller than the rubidium value, indicating that our system is less sensitive to external electric fields. The strong directional dependence for the $47s$ Rydberg state of erbium, along with its short lifetime, requires further investigation and may be attributed to the anisotropic submerged-shell structure.

# Chapter 4

# Sub-Doppler cooling

The ability to cool atoms to their motional ground state is a fundamental requirement for many advanced applications in quantum science and technology. Sideband cooling is a powerful technique that allows atoms to be prepared in their lowest vibrational state within a trapping potential. By reducing the thermal motion of atoms, sideband cooling not only increases the precision of quantum control but also minimizes motional decoherence, which is essential for applications involving highly sensitive quantum states, such as Rydberg states.

In our experiment, we aim to use the 841 nm transition to implement sideband cooling. However, since our system does not satisfy the "magic condition" [24, 39] for this wavelength, which is a key requirement for conventional sideband cooling, we explored an alternative approach usually referred to as chirp cooling [40]. This technique involves dynamically tuning the laser frequency to efficiently remove motional energy from the atoms.

In the final part of this Chapter, we present the preliminary steps toward the implementation of chirp cooling in our setup, such as the reactivation and locking of the 841 nm laser, and the identification of the corresponding resonance.

## 4.1 Sideband cooling

At finite temperatures, atoms in a trap possess non-zero kinetic energy, leading to Doppler shifts and thermal dephasing.

The thermal motion of atoms results in a distribution of velocities, causing a Doppler shift in the resonant frequency. For an atom moving with velocity $\vec{v}$, the effective detuning becomes:

$$\Delta'_{eff} = \Delta_{eff} - \vec{k} \cdot \vec{v}, \tag{4.1}$$

where $\vec{k}$ is the wavevector of the driving field. Thus, a thermal ensemble of atoms with a Maxwell-Boltzmann velocity distribution, experiences an inhomogeneous distribution of detunings $\Delta'_{eff}$. As the temperature increases, the spread of atomic velocities becomes larger, resulting in stronger fluctuations of the effective detunings, that leads to a distribution of Rabi frequencies and consequently to decoherence.

To reduce the effects of thermal motion, we aim to cool the atoms as close as possible to their motional ground state. While standard Doppler cooling methods (such as Zeeman slowing and MOT) allow us to reach temperatures near the Doppler limit:

$$T_D = \frac{\hbar\Gamma}{4k_B} \frac{1 + (2\Delta/\Gamma)^2}{2|\Delta|/\Gamma}, \tag{4.2}$$

where $\Gamma$ is the natural linewidth of the cooling transition, and $\Delta$ is the detuning of the laser frequency from resonance. Further cooling requires techniques capable of surpassing this limit. In order to achieve lower temperatures we need to use Sub-Doppler cooling techniques, like sideband cooling. This technique leads the atom to its motional ground state.

Optical tweezers potential could be approximated as a harmonic potential where the energy levels are given by:

$$E_{g,n} = \hbar\omega_g \left(n + \frac{1}{2}\right),$$

for an atom in the electronic ground state. Similarly for the excited state:

$$E_{e,n} = \hbar\omega_e \left(n + \frac{1}{2}\right),$$

where $\omega_g$ and $\omega_e$ are the trap frequencies for the ground and excited states, respectively. In optical tweezer traps, the confinement is generally anisotropic, leading to two distinct trap frequencies: a lower axial frequency ($\omega_z$) along the propagation direction of the beam, and a higher radial frequency ($\omega_r$) in the transverse plane. Since sideband cooling rely on the laser being detuned by the trap frequency of the targeted motional mode, it is essential to specify which frequency is considered. In the following discussion, we focus on $\omega_r$. This choice is motivated by the fact that the radial confinement is typically much stronger, resulting in larger sideband splittings that are easier to resolve experimentally. Moreover, the corresponding cooling dynamics are faster and less sensitive to technical noise compared to the axial direction. These frequencies are usually of the order of magnitude of tens to hundreds of kHz, and depend on the states' polarizabilities and on the trapping wavelength. However, the same principle can also be applied to cooling the vibrational modes along the axial ($z$) direction, provided that the axial trap frequency $\omega_z$ is sufficiently large and the sidebands in that direction are spectrally resolved. While this is often more challenging due to weaker confinement and smaller motional level spacings, it remains a viable extension for full three-dimensional cooling.

As illustrated in Figure 4.1, sideband cooling is only effective under magic trapping conditions, where the trap-induced level shifts are identical for both ground and excited states. In this scenario, transitions between states like $|g, n\rangle \to |e, n-1\rangle$ can be selectively driven — with the same laser frequency for each $n$ — followed by spontaneous emission that, in the Lamb-Dicke regime, preserves the motional quantum number, gradually cooling the atom to $|g, 0\rangle$.

However, in our current configuration with a 486 nm tweezer, such a magic condition is not fulfilled for the 841 nm transition. As a result, standard sideband cooling is ineffective, since the transition frequencies shift with each motional state

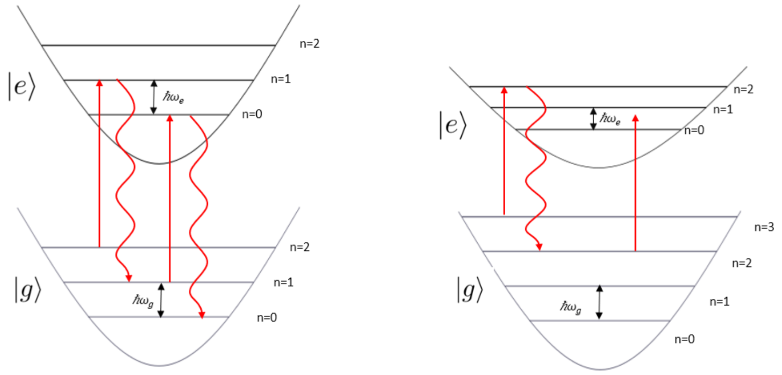

Figure 4.1: When the trap-induced light shifts are the same for the ground and excited states (i.e., $\omega_e = \omega_g$), the transition frequency remains unchanged across motional states, allowing sideband cooling to be performed at a fixed laser frequency. In contrast, if $\omega_e \neq \omega_g$, the energy difference between vibrational levels depends on the electronic state, and the cooling transitions become detuned, reducing cooling efficiency.

and cannot be addressed by a single laser frequency. To overcome this limitation, we adopt a chirp cooling technique [40]. Instead of fixing the laser frequency, the detuning is dynamically swept (chirped) to remain resonant with the changing sideband frequencies as atoms cool. This method allows us to effectively reduce the atomic kinetic energy even in non-magic traps.

### 4.1.1 Sideband cooling without magic condition

Unlike standard sideband cooling, which works under magic trapping conditions ($\omega_e = \omega_g$), chirp cooling works instead in the case of $\omega_e < \omega_g$.

The idea is to apply a controlled frequency chirp to the cooling laser. The laser detuning is ramped from a large red detuning (around $\delta \approx -6 \cdot \omega_g$) towards $\delta \approx -\omega_g$, over a timescale of approximately 10 ms. The chirp must be slow enough to allow spontaneous emission after each absorption event, ensuring that the atom loses motional quanta step by step until it reaches the trap ground state.

As illustrated in Figure 4.2, chirped sideband cooling enables ground-state cooling even when the polarizability of the ground state $\alpha_g$ is larger than that of

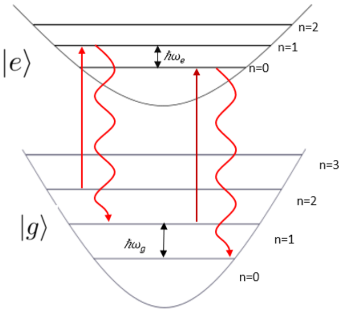

Figure 4.2: If $\omega_e < \omega_g$, the transition frequencies vary with the motional quantum number $n$, requiring a dynamic tuning of the laser frequency to continue cooling effectively.

the excited state $\alpha_e$, such that $\omega_g > \omega_e$. In this situation, the excited state experiences a shallower trapping potential than the ground state, and a fixed-frequency laser cannot remain resonant with all sideband transitions. The frequency chirp compensates for this mismatch, enabling a cascade of cooling transitions.

This is precisely the situation we face with the 841 nm transition in erbium. As shown in Figure 4.3, the polarizability of the excited state at 841 nm is significantly lower than that of the ground state at our tweezer wavelength of 486 nm. Therefore, $\omega_g > \omega_e$, and standard sideband cooling is not feasible. This physical configuration makes the 841 nm transition a candidate for chirped sideband cooling.

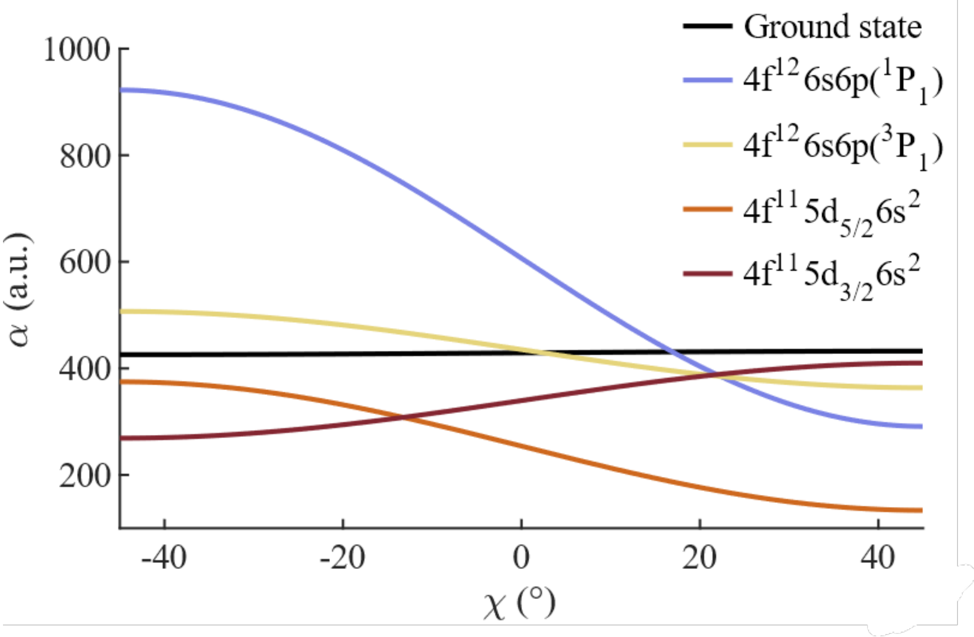

Figure 4.3: Calculated polarizability of erbium for the ground and excited states relevant to the 841 nm transition, as a function of wavelength. At the tweezer wavelength of 486 nm, the ground state is more strongly trapped than the excited state, i.e., $\alpha_g > \alpha_e$, black and orange respectively. This condition requires the use of chirped sideband cooling rather than standard sideband techniques. The plot also shows the polarizability of the excited states of erbium at 401 nm, 583 nm and 1299 nm.

## 4.2 841 nm ECDL

In order to achieve the sub-Doppler cooling regime we decided to use the narrow 841 nm transition of erbium. Our 841 nm laser is a homemade external-cavity diode laser (ECDL). In this section, I will describe the process of initial set up and frequency locking of this laser.

The ECDL is designed to operate in single-frequency mode and consists of the following main optical components (see Figure 4.4):

- LD (Laser Diode): a laser diode without AR coating, that serves as the gain medium. It emits a broad spectrum centered around the nominal wavelength of 852 nm. L852P100 852 nm from Thorlabs

- CL (Collimating Lens): an aspheric lens, it collects and collimates the divergent light emitted by the diode. A230TM-B from Thorlabs.
- IF (Interference Filter): a narrowband interference filter, tilted by an angle $\theta$. It acts as the wavelength-selective element, replacing the diffraction grating used in traditional Littrow setups. The spectral selection is highly sensitive to the tilt angle. 852 nm Interference Filter from Radiant Dyes Laser & Acc.
- $L_1$: a lens that focuses the light transmitted through the filter toward the external cavity. A230TM-B from Thorlabs.
- PZT (Piezoelectric Transducer): a piezoelectric actuator mounted behind the partially reflective mirror (OC). It allows fine tuning of the external cavity length, enabling precise frequency control. Piezoceramic Rings by piceramic.
- OC (Output Coupler): a partially reflective mirror that closes the external cavity and allows extraction of the laser beam. Its reflectivity is optimized to balance feedback and output power. 20% reflectivity Output Coupler 108216 by layertec.
- $L_2$: a final collimating lens that shapes the output beam. A230TM-B from Thorlabs.

The interference filter (IF) selects a narrow wavelength band from the diodes emission. Light transmitted through the filter is partially reflected by the output coupler (OC) and fed back into the laser diode. This wavelength-selective optical feedback narrows the laser linewidth and enables single-mode operation. The external cavity length, controlled via the PZT, allows fine frequency tuning of the emitted light and will be discussed in more detail later. The laser is finally controlled via a laser driver and temperature PID that allows us to change the current and temperature on the laser diode.

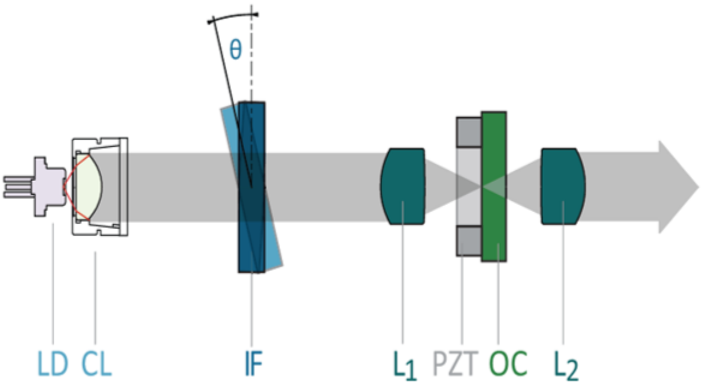

Figure 4.4: Optical setup of an ECDL in cat-eye configuration. The laser diode (LD) is mounted together with an aspheric lens (CL) inside a collimation tube, which is also thermally in contact with the LD and a thermal control. The collimated beam is guided through a narrow passband interference filter (IF), which is mounted on a rotation stage for coarse wavelength selection. The cat-eye reflector is formed by the cat-eye lens ($L_1$) and the outcoupler (OC), i.e. a partially reflective mirror. To enable cavity length tuning the cat-eye reflector is fitted on a piezoelectric transducer (PZT), whereas the distance between $L_1$ and OC remains fixed. Another lens ($L_2$) finally collimates the beam before laser output.

Initially, the power output was really unstable and fluctuating from 2 to 15 mW. I realized that the LD was broken and changed it. I simply replaced the LD with a new L852P100 852 nm from Thorlabs that is the same that was already used. This LD is not AR-coated, introducing another cavity, limiting its tunability, but also making it easier to work in a single-mode regime. Indeed, we were not able to see a single-mode behavior with an AR coated LD, so we decided to go for the Thorlabs one.

The laser frequency is not only determined by the transmission window of the IF, but it is also correlated to the LD gain profile, the LD cavity, and the external cavity formed with the OC mirror. In Figure 4.5 the transmission of each component as well as the gain profile of the LD are shown.

To change the frequency of the ECDL, the following parameters can be used:

- LD temperature ($T_{LD}$);

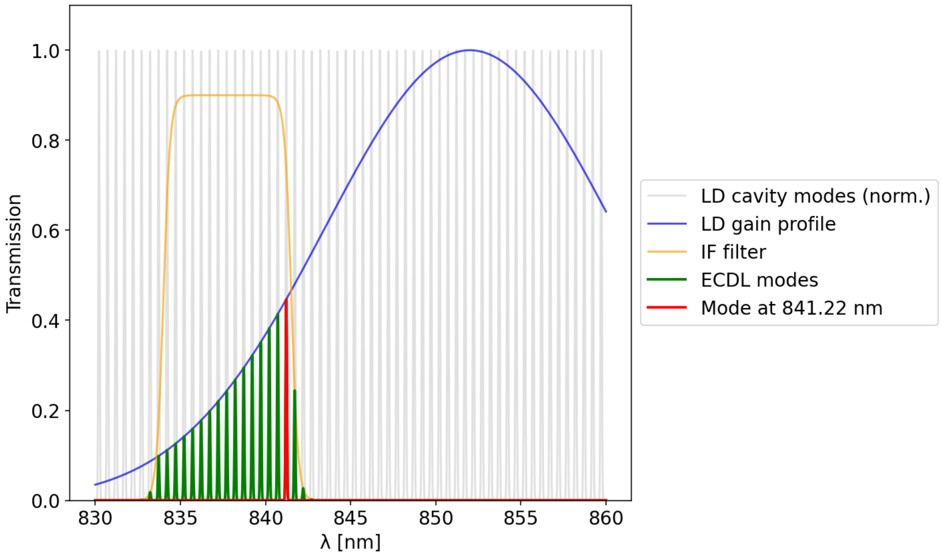

Figure 4.5: The transmission of each part together with the gain profile reveals the most favourable lasing mode (red line). The IF is rotated to a center wavelength of 841.23 nm. Thereby it is clearly visible that a sharp edge of the IF is more important than a narrow bandwidth. Additionally the finite slope of the gain profile, approximated by a Gaussian function, is of prime importance too. Further due to the narrow gain bandwidth of GaN diodes, the LD needs to be well chosen to fit the desired wavelength region without utilizing extreme LD temperatures. Due to the small FSR of the external cavity the modes are not distinguishable in this graphic.

- LD injection current ($i_{LD}$);
- the mirror spacing of the external cavity, via a voltage ($V_{pzt}$) applied to a PZT;
- the IF angle $\theta_{IF}$.

These parameters act on different time scales, from fast to slow: $i_{LD}$, $V_{pzt}$, $\theta_{IF}$, $T_{LD}$ [41].

The transmission window of the IF at normal incidence can be shifted to shorter wavelengths by increasing the angle of incidence $\theta_{IF}$.

After replacing the diode, alignment on the OC was necessary to restore lasing in the ECDL. Alignment has been made by manually moving the LD case making sure the light was going through the IF and into the OC. Once this was performed, we maximized the laser injection by moving the lens $L_1$ and focusing the beam into the OC. To maximize the injection we were looking at the power on the powermeter placed at the output of the ECDL. We also measured the PI curve of the laser (see Figure 4.6).

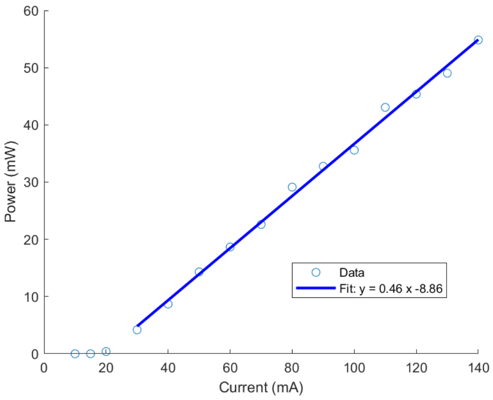

Figure 4.6: PI curve of the laser diode. The output power is shown as a function of the injection current. Below a certain threshold current, the emission is dominated by spontaneous emission and grows slowly, while above the threshold the diode enters the stimulated emission regime, resulting in a linear increase of output power with current.

Also the beam shape and waist out of $L_2$ was different because of the new LD and alignment, requiring partial modification of the existing beam path, as shown in Figure 4.7.

Using the $L_2$ lens, we focused the laser beam into the optical isolator to minimize losses within the device. After this step, we implemented a telescope to collimate the beam and used the cylindrical telescope, previously employed, to reshape the beam from an elliptical to a Gaussian profile. Due to the rectangular geometry of the active region in a laser diode, the emitted beam typically has an elliptical shape. The diodes active region is much wider in one direction than in the perpendicular direction, resulting in a beam with different divergence angles along the two axes. Our beam path is configured to provide three distinct outputs:

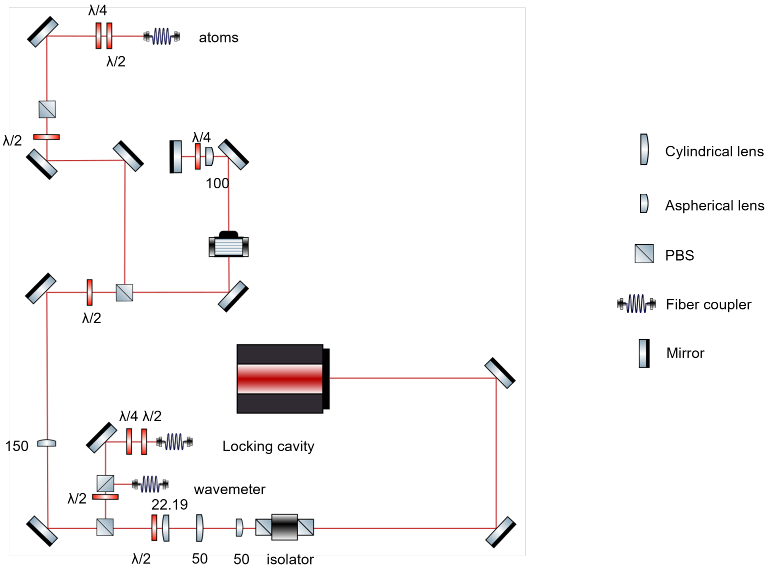

Figure 4.7: Optical path of the 841 nm laser beam. The laser frequency is continuously monitored by a wavemeter, stabilized via a reference cavity for frequency locking, and the stabilized beam is ultimately delivered to the atoms.

a wavemeter to monitor the laser wavelength, a cavity to lock the laser in order to have a wavelength stable and close to resonance, and finally, the atoms.

Once the optical setup was complete, we verified the laser wavelength using the wavemeter. By exploiting the degrees of freedom described earlier, we fine-tuned the laser until it reached the desired wavelength of 841.223 nm.

At this point, we locked the laser to the resonance frequency of 841.2238 nm using the PDH locking technique, as detailed in B. Fine-tuning and scanning around this frequency were made possible by an acousto-optic modulator (AOM) in double-pass configuration, installed before the beam reaches the atoms.

## 4.3 Experimental results

We started doing some preliminary experiments, in order to perform chirp cooling using the 841 nm transition. As a first step, we identified the atomic resonance, whose frequency had already been determined from previous measurements performed in our laboratory. The spectroscopy was carried out in a multi-atom regime, so we did not apply LACs after loading the tweezers. Following the usual tweezer loading, we applied an 841 nm loss pulse of 100 ms duration and 0.2 mW power before performing imaging at 401 nm. The spectrocopy results are shown in Figure 4.8. The $\sigma^-$, $\pi$ and $\sigma^+$ transitions are splitted due to the 10 G magnetic field applied along the $z$-direction during the whole sequence. The Clebsch-Gordon coefficients of each transition are shown in Figure 4.9.

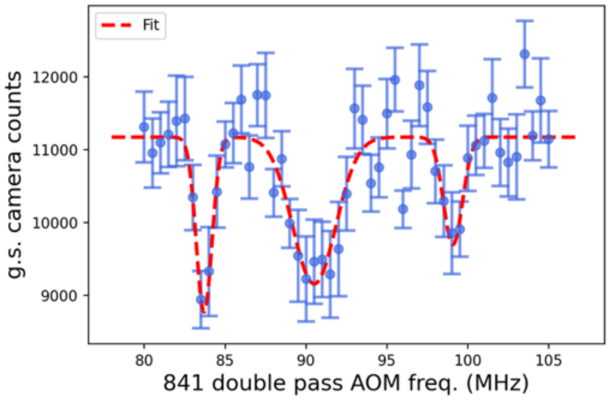

Figure 4.8: Resonances of the 841 nm transition in the presence of a 10 G magnetic field applied along the $z$-axis. Due to the horizontal polarization of the 841 nm light, the atoms couple to both $\sigma^-$ and $\sigma^+$ transitions, as well as to the $\pi$ transition, the latter arising from a small residual vertical polarization component introduced by imperfections of the $\lambda/2$ waveplate. The laser frequency is tuned by means of a double-pass AOM, starting from a base wavelength of 841.22384 nm. In both passes the +1 diffraction order is selected, resulting in a net +2 order. Accordingly, the frequency shift is twice the applied AOM drive frequency, which is the value reported on the horizontal axis.

Subsequently, we performed light-shift measurements, repeating the same spectroscopy measurement for different tweezer powers, in order to estimate the shift of the resonance frequency, focusing on the $\sigma^-$ transition (see Figure 4.10). Increasing the tweezer power is required in order to reach a radial trap frequency of the ground state $\omega_g$ much larger than the natural linewidth of the transition ($\frac{\Gamma}{2\pi} \approx 8$ kHz). The experimental goal was therefore to increase the tweezer power

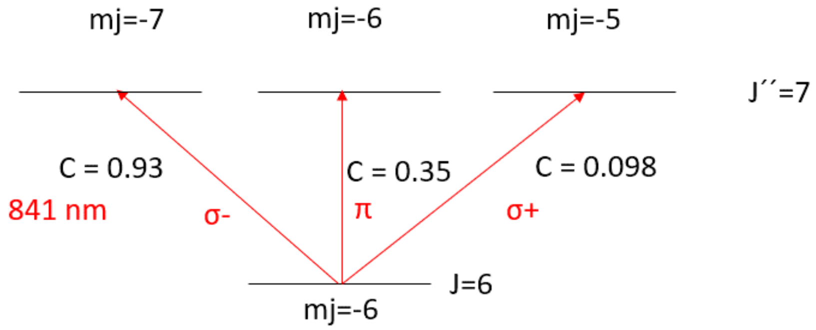

Figure 4.9: Transitions from the ground state to an excited 841 nm state, with the relative Clebsch-Gordon coefficients.

by a factor of 10, which leads to an increase of $\omega_g$ by a factor of $\sqrt{10}$. Indeed:

$$\omega_r \propto \frac{\sqrt{P}}{w_0} \tag{4.3}$$

where $P$ is the power of the tweezer light and $w_0$ is the waist. This makes clear that to increase the trapping frequency $\omega_r$ for both the ground and the excited state, we can either increase the power of the tweezer or reduce the waist. For a tweezer power of 1.8 mW and waist of 0.8 $\mu$m the radial trapping frequency is $\omega_g \approx 37$ kHz.

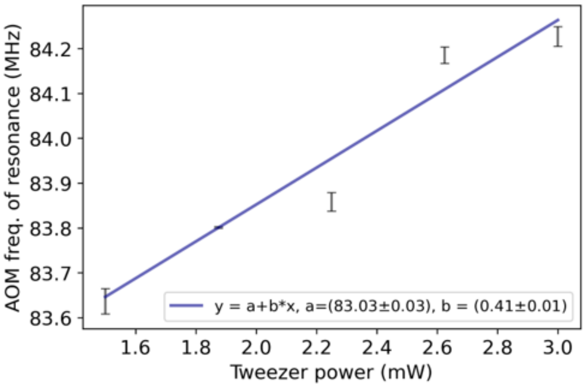

Figure 4.10: Light-shift measurements of the 841 nm $\sigma^-$ resonance as a function of tweezer power. From the linear fit, the resonance frequency at a tweezer power of 18 mW was estimated.

The resonance frequency is linearly proportional to the tweezers power, hence performing a linear fit we determined the resonance frequency at 18 mW of power for each tweezer (Figure 4.10), and tried to see it without success. The main limitation was that, when the tweezer power is significantly increased, more atoms are loaded into the trap since in this measurement we did not apply LACs. The outer atoms experience a lower effective intensity and therefore a reduced light shift. As a result, the resonance broadens and becomes asymmetric, which prevents efficient chirp cooling, as shown in Figure 4.11.

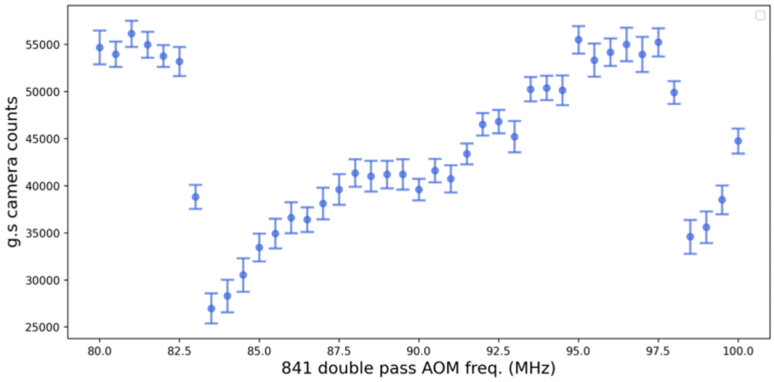

Figure 4.11: $\sigma^-$ transition for 18 mW of tweezer power. The resonance shows a big broadening and asymmetry.

A possible solution to this issue would be to operate in the single-atom regime, or alternatively to reduce the tweezers waist on the atoms, which would increase $\omega_g$ without requiring higher optical power. In conclusion we can say that we established the basis for implementing more advanced cooling schemes in our system.

# Chapter 5

# Conclusion and Outlook

In this thesis, we have explored the experimental foundations for controlling erbium atoms in highly excited Rydberg states, with a particular focus on electric field stabilization and sub-Doppler cooling techniques. These two aspects represent essential building blocks for future quantum simulation platforms based on lanthanide atoms.

In our experimental scheme, Rydberg excitation is achieved through a two-photon transition. The first photon couples the ground state to an intermediate excited state, while the second photon drives the transition to the desired Rydberg level. However, since the first photon is strongly red-detuned from resonance, the population of the intermediate state remains negligible. This allows us to effectively treat the system as a two-level atom directly coupled to the Rydberg state.

For quantum simulation purposes, it is crucial to maintain full control over the atomic system. In particular, coherent oscillations between the ground and Rydberg states must be sustained for times longer than the duration of the simulated dynamics. Achieving and preserving coherence over such timescales requires precise control of both external fields and atomic motion.

A central result of this work is the implementation and characterization of electric field control. The extraordinary sensitivity of Rydberg states to external perturbations makes the compensation of stray fields indispensable. Indeed, we show that stray electric fields arising from the surrounding environment reduce the coherence of our system. By employing dedicated electrodes and custom-designed driving electronics, we were able to manipulate and stabilize the electric field. Moreover, we extracted information about the static polarizability of the $47s$ Rydberg state. These studies confirmed the high sensitivity of Rydberg states to external electric fields, but also indicate that further investigations are needed, particularly regarding the submerged-shell anisotropy, which is a distinctive feature of lanthanide atoms such as erbium.

In parallel, we investigated sub-Doppler cooling strategies for erbium. Achieving lower atomic temperatures is another crucial requirement for extending coherence times. Narrow-line cooling on the 841 nm transition was identified as a particularly promising route. At first, we fixed the external cavity diode laser intended to use for this transition. The laser was locked using the PDH technique, and preliminary measurements of the atomic transition frequency were performed.

The results presented in this thesis establish a solid groundwork for the precise control of erbium atoms in the ultracold regime, focusing on electric field control and sub-Doppler cooling as techniques to improve the coherence time of the system. Looking ahead, further development of sub-Doppler cooling techniques and refined electric field compensation will pave the way toward the realization of large-scale quantum simulators using Rydberg atoms. Such platforms will open unique opportunities to explore complex quantum phenomena that remain intractable with classical computational methods.

# Appendix A

# Electronic Circuitry and Setup Characterization

In this appendix, we describe the electronic circuitry of the components used to control the hardware, including electrodes, lenses and MCPs. All circuits and components were designed and manufactured by the electronic workshop of the IQOQI. Consequently, I characterized each component, to ensure a full understanding of its behavior before the implementation in the experiment.

## A.1 HV-LV Switch Box

Each HV-LV Switch Box, shown in Figure 2.6, contains a high-voltage, high-speed MOSFET push-pull switch that selects the voltage supply for a field plate between high and low voltage. The switches used are the HTS 41-02-HB-LC-C, manufactured by Behlke, with the options S-TT (soft transition time) and LP (low pass). These options ensure reduced sensitivity to high-frequency noise. The switch can transition from 0 to 4 kV in 30 ns with a delay of 200 ns and has a low on-resistance of $R_{\text{on}} = 16\,\Omega$. It is also capable of switching to negative high voltage.

To ensure proper operation, the negative input must always be lower than the positive input. For this reason, each switch box is configured in one of two ways, as shown in Figures A.1 and A.2. The version designed to switch negative high voltage has its SHV connectors leading to the -HV input of the switch, while the version designed to switch positive high voltage has its SHV connectors leading to the +HV input of the switch.

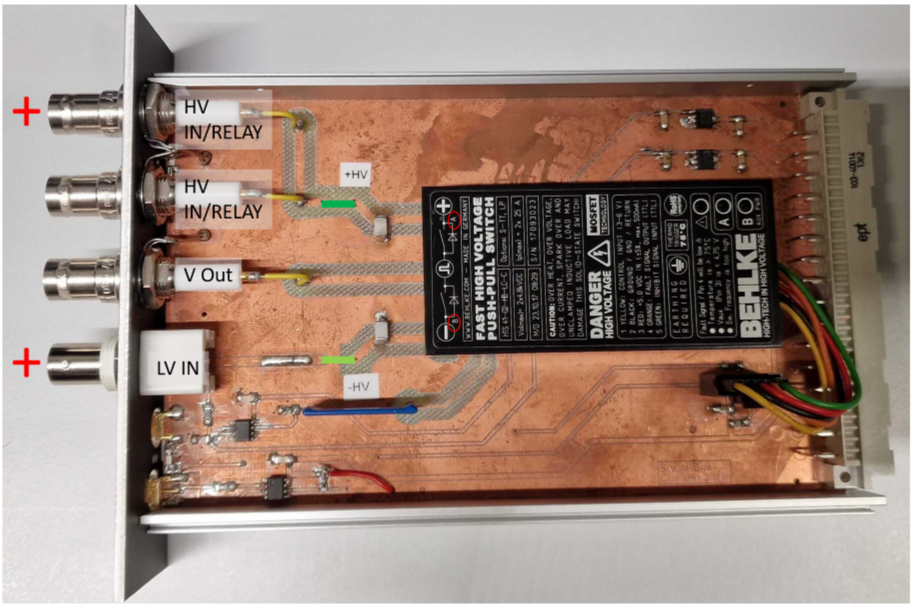

Figure A.1: Configuration of the HV-LV Switch Box for positive high voltage. The positive HV is connected to the positive pole of the MOSFET, while the LV to the negative pole.

The basic schematic of the switch box is shown in Figure A.3. The output voltage monitor is connected to the SMA2 connector, where the high-voltage output divided by 1000 is provided. Three high-voltage capacitors (4 pF, 40 pF, and 400 pF) are connected in parallel between the inputs of the switch to store charge and ensure that the voltage supply can provide the required current without delays. These capacitors counteract potential drops in the supply voltage.

The first test of the switches involved applying a TTL signal (05 V square wave) to verify their behavior. The switches are configured in active high mode, meaning that the HV output is enabled when the TTL signal is high (5 V). Figure

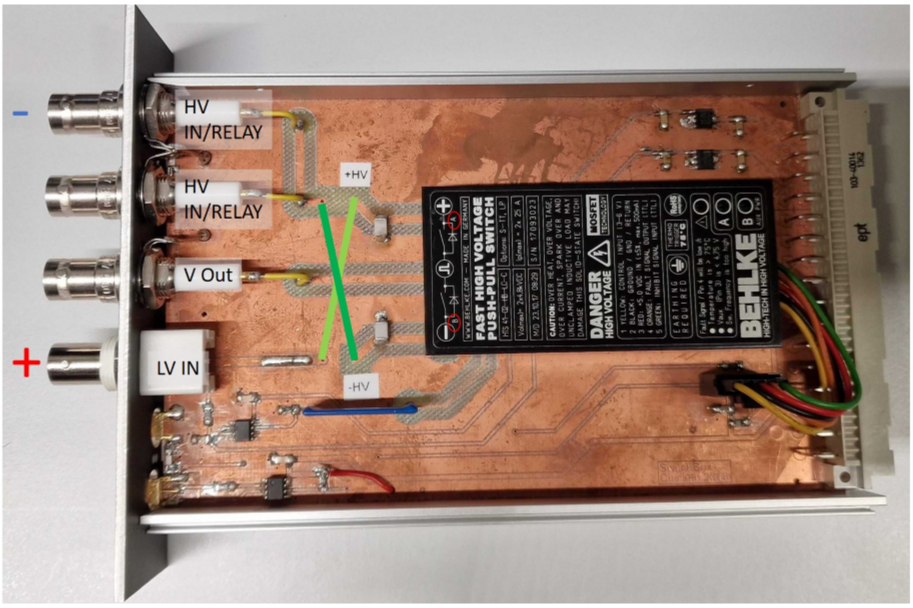

Figure A.2: Configuration of the HV-LV Switch Box for negative high voltage. The negative HV is connected to the negative pole of the MOSFET, while the LV to the positive pole.

A.4 shows the behavior of the switch under these conditions.

Initial tests were conducted with lower voltages (300 V) to minimize risks. Using an RS Pro HV generator with an amplification factor of 300, we observed significant ringing and a slow rise time of approximately 200 $\mu$s, as shown in Figure A.5. This behavior indicates that the HV amplifier was too slow to meet the switch's requirements, limiting its performance.

To address this issue, we switched to an ISEG HV generator, also set to 300 V. This improved the rise time to 2.5 $\mu$s, as shown in Figure A.6, though it remained slower than the MOSFET switching time. This suggests that the HV generator remains a limiting factor for the switch's performance.

The behavior of the negative HV switches was tested and showed similar rising time of the positive HV switches. Figure A.7 shows the signal observed on the oscilloscope for the negative HV configuration.

During our experiments, we also noticed that when connecting the switch cards to a rack that is linked to the bus system, unexpected behaviors are observed on the other cards in the same rack. In particular, some analog channels change their set values, and digital outputs show oscillations around 5 V. To avoid such interference, it is recommended to isolate the switch cards from the bus system by placing them on a dedicated rack that doesn't have bus system connection. This approach is convenient since these cards do not require any configuration via MATLAB, but only external inputs.

## A.2 Lens Box

The Lens Boxes, shown in Figure 2.6, provide the voltages for the two electrostatic lens systems and the wire grid in front of each MCP detector. They amplify the input voltages and switch the output on the rise of a TTL signal. When the TTL signal is low, the four lens outputs are grounded to prevent interference during the experiment. The fifth input voltage for the wire grid is fed directly into the output connector and remains active at all times. The schematic of the Lens Box is shown in Figure A.8.

Testing confirmed that the lens outputs are active only during the ionization pulse (TTL high). Figure A.9 shows the behavior of one lens output, where an input of -10 V results in an output of approximately +70 V, corresponding to a gain of -7. We observed that a positive input resulted in a negative output (gain = -7). After consulting with our electronic workshop, we tested the opposite configuration, which was more intuitive but resulted in significantly higher noise levels. Since we need to compensate any stray electric field, we desire the lowest level of noise when TTL is low (0 V) and then we decided to stick with this configuration. The rising time was also measured and found to be approximately 9 $\mu$s.

The wire grid outputs were verified to remain active throughout the experiment, regardless of the TTL signal. A positive input corresponds to a positive output on the wire grids, as shown in Figure A.10.

## A.3 MCP Supply Boxes

The MCP Supply Boxes, shown in Figure 2.6, contain a high-voltage divider circuit to provide the appropriate voltages for the MCP detectors. A series of high-voltage resistors generates different voltage levels from a single input voltage. Depending on whether the MCP is used to detect ions or electrons, the resistor configuration and connections differ. The schematic of the MCP Supply Box is shown in Figure A.11.

For positive ion detection, the MCP requires a negative high voltage, with a voltage divider providing -3 kV at MCP-IN, -0.5 kV at MCP-OUT, and ground at the anode. For electron detection, the MCP requires a positive high voltage, with a voltage divider providing 0.5 kV at MCP-IN, 2.5 kV at MCP-OUT, and 3 kV at the anode. In the latter case, a high-pass filter, consisting of a 100 pF capacitor and a 1 M$\Omega$ resistor, is used to extract the detector signal from the DC high voltage. Note that in the case of positive ions, the anode is at ground and provides the detector signal directly. It does not require a connection to the supply box. Testing confirmed the presence of the required voltage gradient to accelerate secondary emission electrons.

The behavior of the MCP for electron detection is shown in Figure A.12, while the behavior for ion detection is shown in Figure A.13.

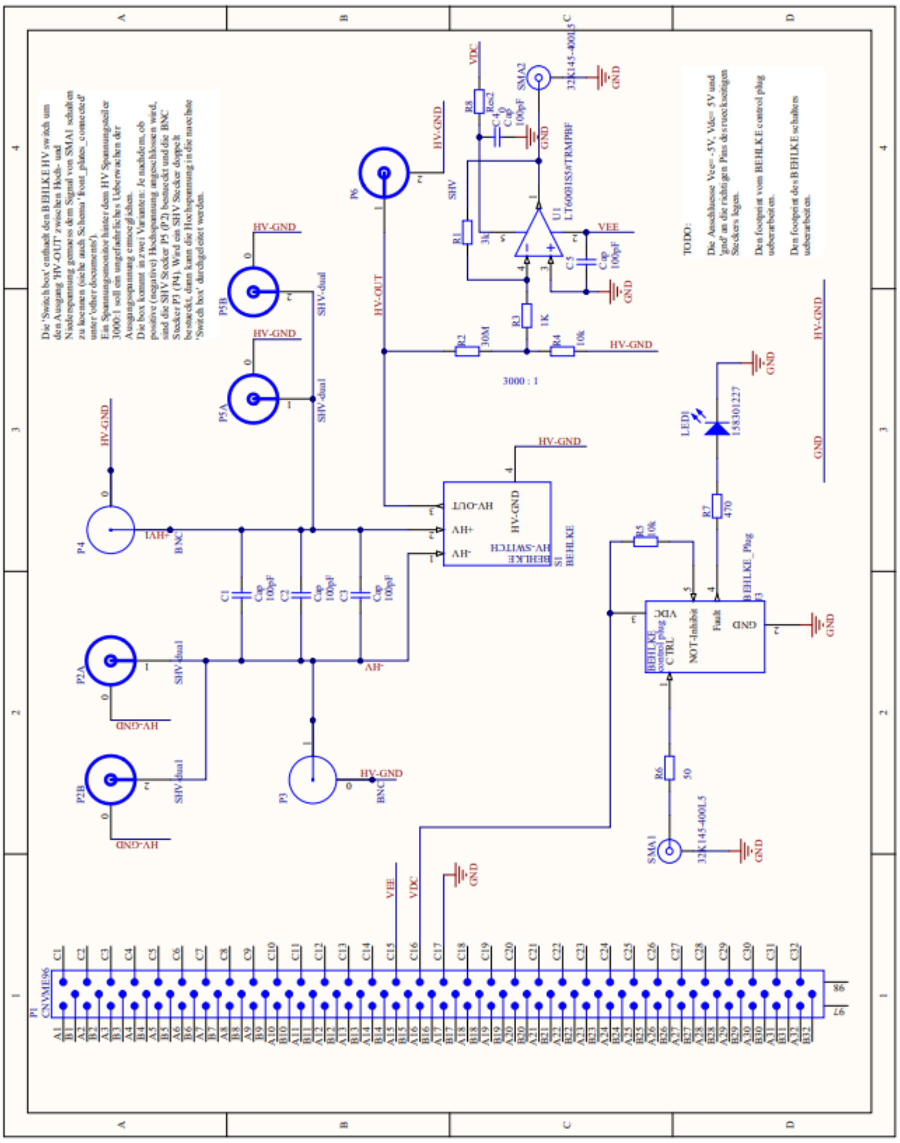

Figure A.3: Schematic layout of the HV-LV Switch Box. The switch connects the field plates (P6) to either the low-voltage supply (P3) or the high-voltage supply (P5). For negative high voltage, P4 and P2 must be used for low and high voltage, respectively. The capacitors (C1-C3) match the capacitance of the field plate to allow fast switching. The switch is triggered by a TTL signal via SMA1, and a voltage divider provides an output voltage monitor at SMA2.

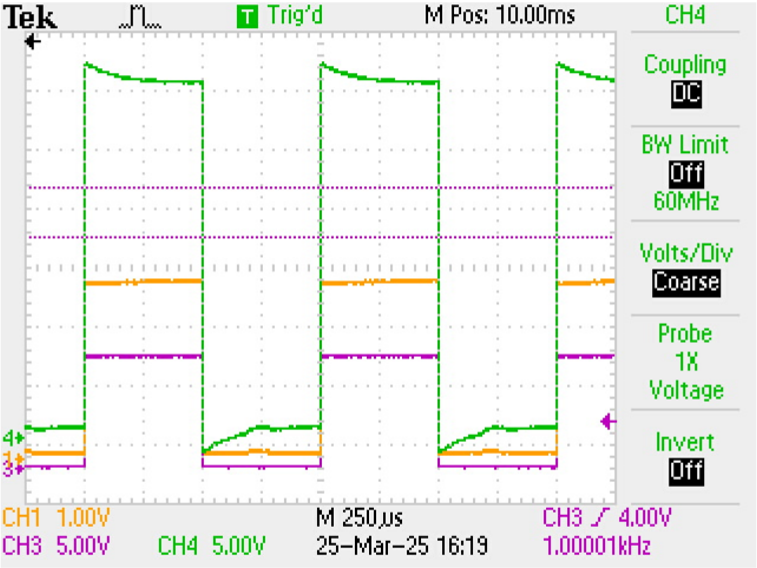

Figure A.4: Behavior of the HV-LV Switch Box in active high mode. The purple trace represents the TTL signal, the green trace represents the HV output, and the yellow trace represents the monitor output.

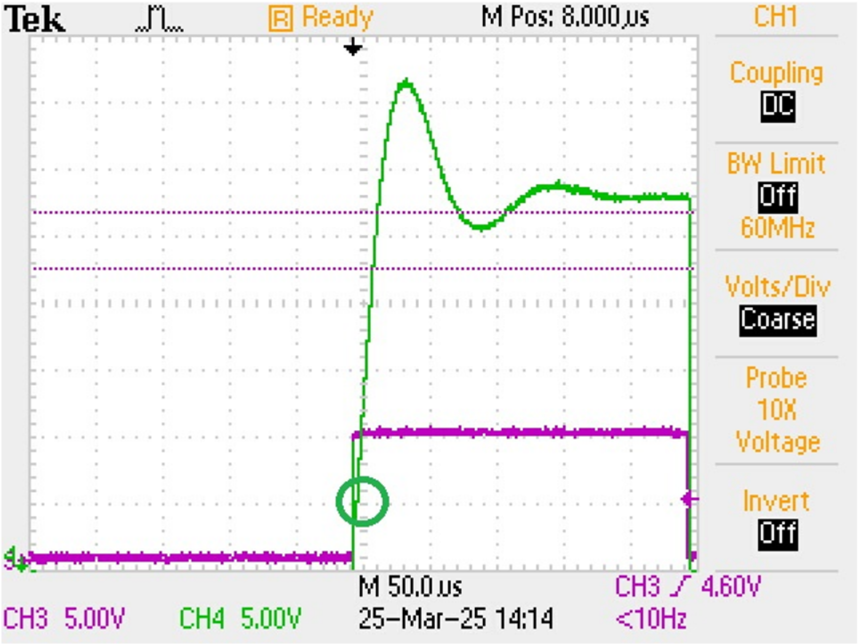

Figure A.5: Slow rise time of the HV output when using the RS Pro HV generator. After 5 $\mu$s, the voltage is still far from its maximum value, around 15%.

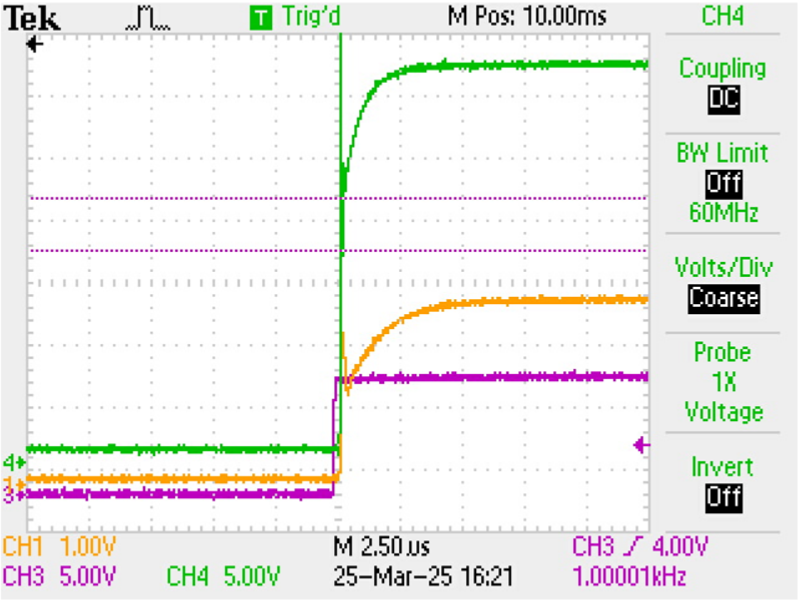

Figure A.6: Improved rise time of the HV output when using the ISEG HV generator. After 5 $\mu$s the voltage is at its maximum value.

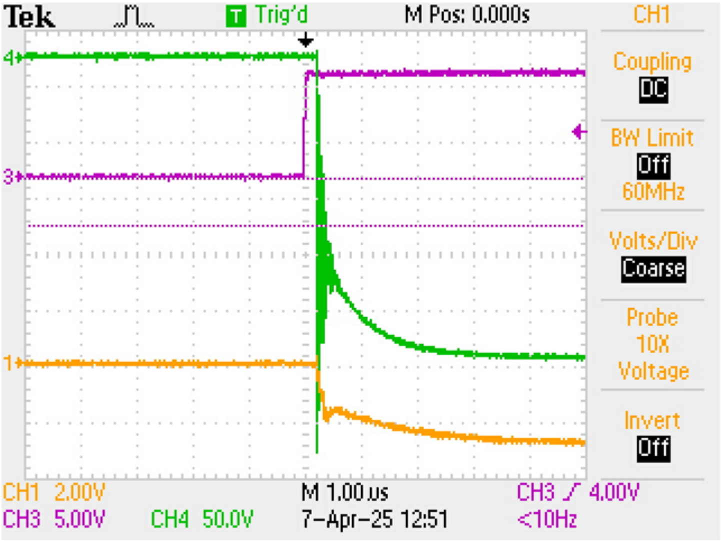

Figure A.7: Oscilloscope signal for the negative HV switch configuration. The rising time is again measured to be around 2.5 $\mu s$

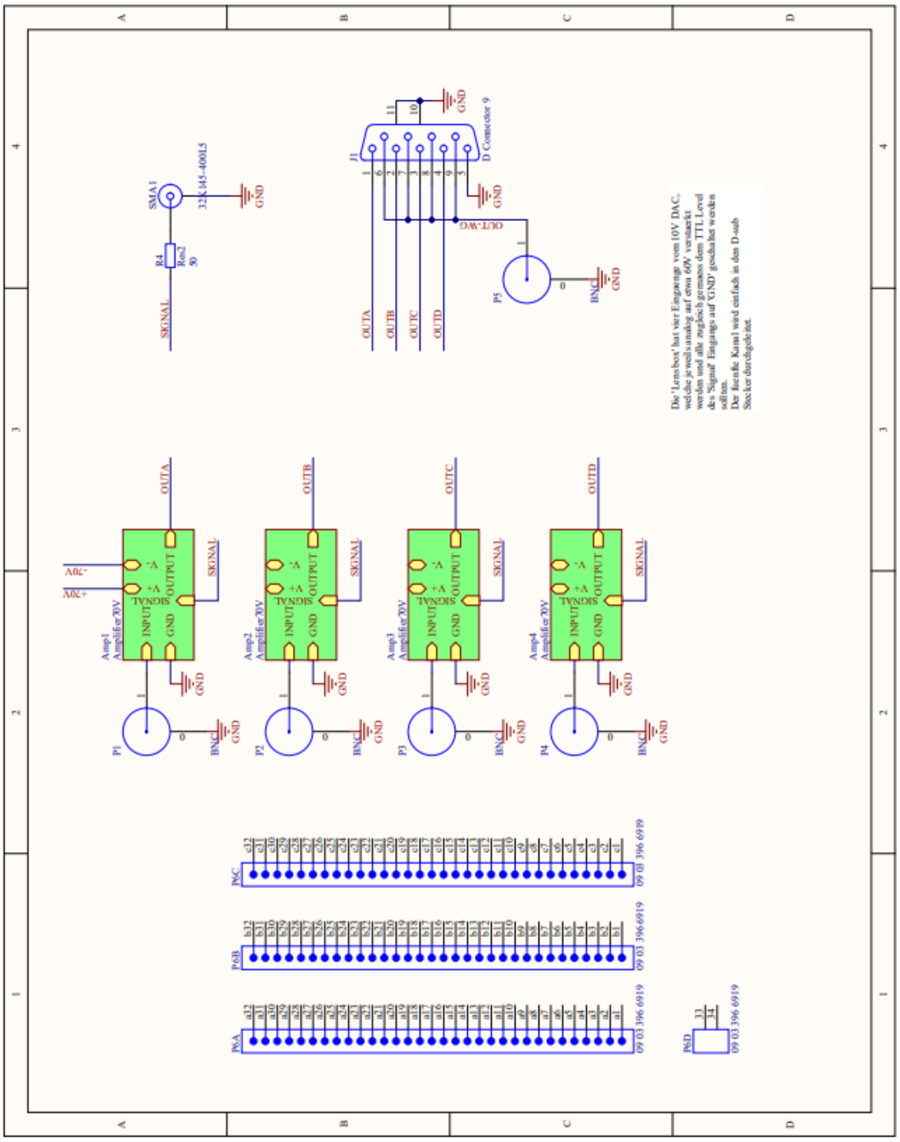

Die 'Lensbox' hat vier Eingaenge vom 10V DAC, welche jeweils analog auf etwa 60V verstaerkt werden und alle zugleich gemaess dem TTL Level des 'Signal' Eingangs auf 'GND' geschaltet werden sollten.
Der fuenfte Kanal wird einfach in den D-sub Stecker durchgeleitet.

Figure A.8: Schematic of the Lens Box. Four input voltages are amplified to ±70 V and switched on when the TTL signal is high. A fifth input is fed directly into the output connector. This way, the five needed voltages are bundled into one cable that connects to the MCP vacuum flange.

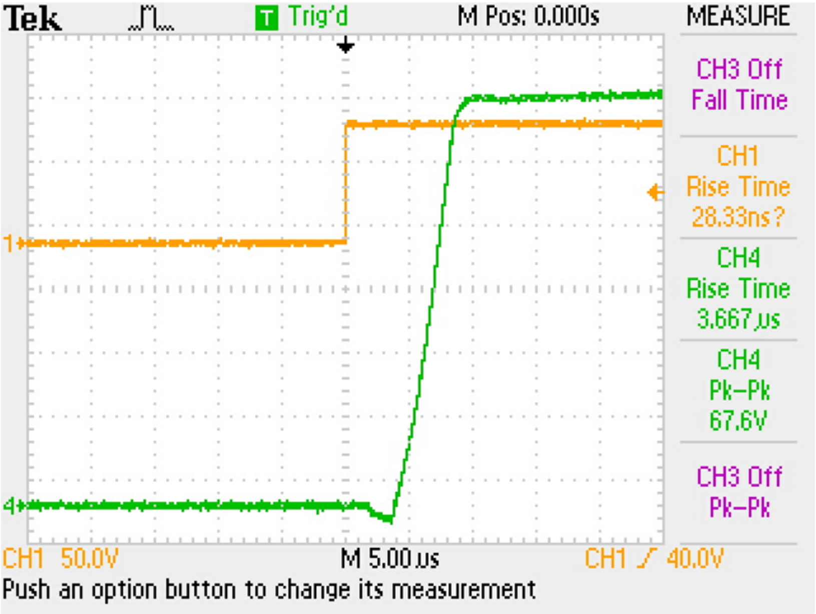

Figure A.9: Behavior of a lens output. An input of −10 V results in an output of approximately +70 V, corresponding to a gain of −7.

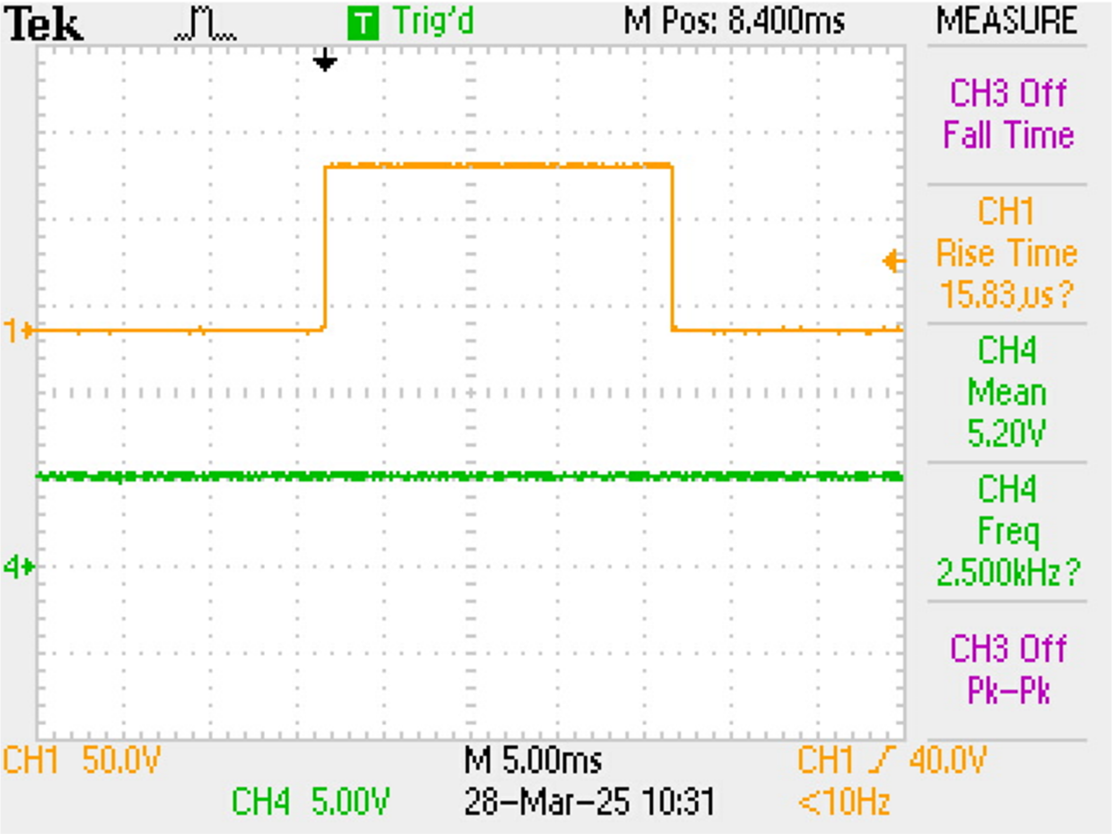

Figure A.10: Behavior of the wire grid output. The output is constant independently on the TTL signal.

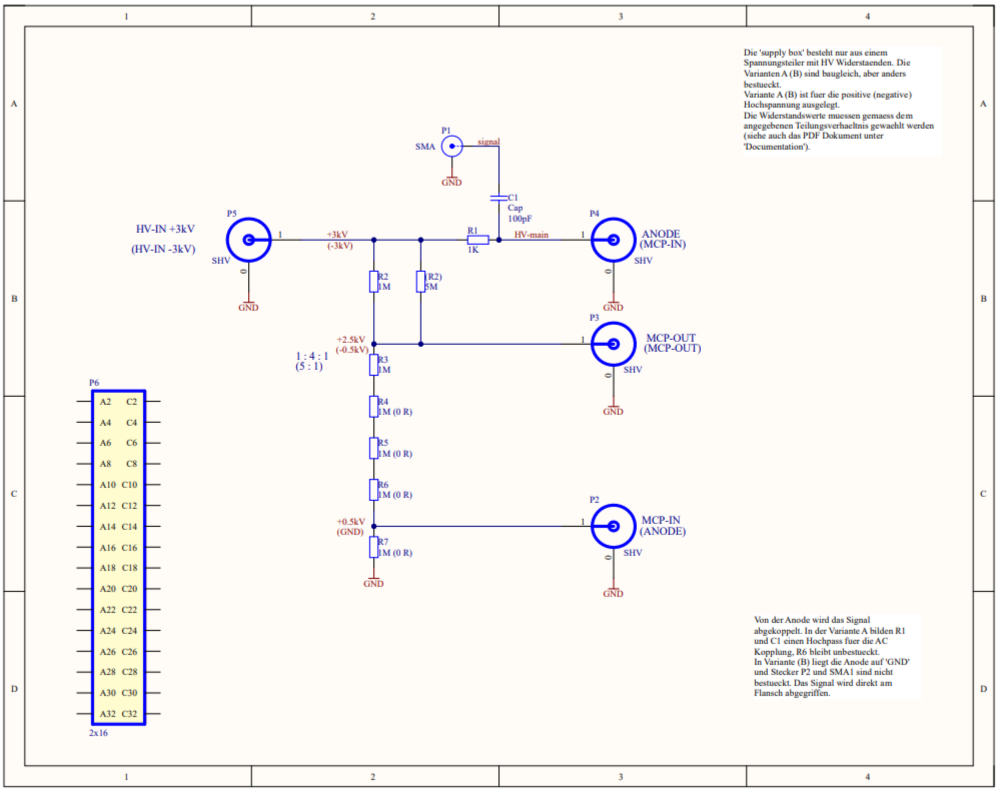

Die 'supply box' besteht nur aus einem Spannungsteiler mit HV Widerstaenden. Die Varianten A (B) sind baugleich, aber anders bestueckt.
Variante A (B) ist fuer die positive (negative) Hochspannung ausgelegt.
Die Widerstandswerte muessen gemaess dem angegebenen Teilungsverhaeltnis gewaehlt werden (siehe auch das PDF Dokument unter 'Documentation').

Von der Anode wird das Signal abgekoppelt. In der Variante A bilden R1 und C1 einen Hochpass fuer die AC Kopplung, R6 bleibt unbestueckt.
In Variante (B) liegt die Anode auf 'GND' und Stecker P2 und SMA1 sind nicht bestueckt. Das Signal wird direkt am Flansch abgegriffen.

Figure A.11: Schematic of the MCP Supply Box. Connections for detecting positive ions are shown in parentheses, while connections for detecting electrons are shown without parentheses.

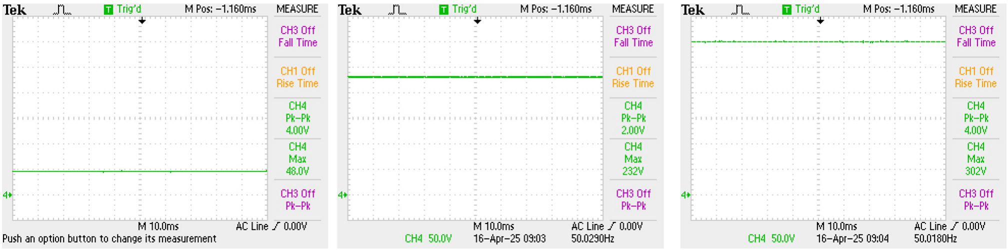

Push an option button to change its measurement

Figure A.12: Behavior of the MCP configured for electron detection. From left to right we can see the output of MCP-IN, MCP-OUT and ANODE. The voltage gradient is necessary to accelerate secondary emission electrons.

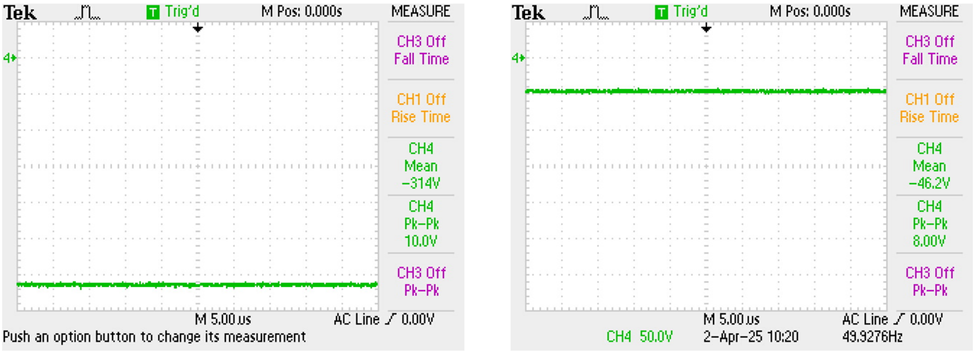

Figure A.13: Behavior of the MCP configured for ion detection. From left to right we can see the output of MCP-IN, MCP-OUT. Here the ANODE can be set to zero and we still have the voltage gradient behavior.

# Appendix B

# PDH locking

## B.1 PDH locking technique

In many precision experiments, such as atomic spectroscopy, quantum optics, and interferometry, the frequency of a laser must be extremely stable and its linewidth narrow. A narrow linewidth ensures coherent interaction between the laser and the system of interest, minimizing frequency noise and maximizing the resolution of measurements. Achieving such precise frequency control is challenging due to environmental noise, thermal fluctuations, and intrinsic laser instabilities.

The Pound-Drever-Hall (PDH) locking technique is a powerful method for stabilizing the frequency of a laser to an optical cavity with high precision. By generating an error signal that is sensitive to the detuning between the laser frequency and the cavity resonance, the PDH method enables real-time feedback to correct for frequency deviations. This technique is widely used in applications requiring ultra-stable lasers, such as gravitational wave detection and quantum technologies [43].

The optical cavity used for the PDH locking of the 841 nm laser is a FabryPerot cavity manufactured by SLS, featuring a ULE (ultra-low expansion) spacer with four bores. The cavity's zero-crossing temperature for the coefficient of thermal expansion (CTE) is measured to be 27.2°C. The FSR of the cavity is approximately 1.5 GHz.

To ensure optimal coupling into the cavity, some alignment steps have been performed. First, we roughly aligned the reflected beam to overlap with the incoming beam, ensuring that the beam hits the cavity perpendicularly. Then we performed a large and slow scan of the cavity piezo to observe the transmitted modes on a camera, making sure that only the gaussian $\mathrm{TEM}_{00}$ mode was visible. Suppressing the other modes also partially suppressed the Gaussian mode. Therefore, we found a compromise to achieve the best possible alignment for the Gaussian mode while maximizing its signal.

The PDH locking scheme relies on phase modulation to extract information about the frequency detuning of the laser from the cavity resonance. The process begins with the phase modulation of the laser beam using a fiber-coupled electro-optic modulator (EOM) (PM830 from Jenoptik), which creates sidebands at frequencies $\nu \pm f_{\mathrm{mod}}$, where $\nu$ is the laser frequency and $f_{\mathrm{mod}}$ is the modulation frequency. These near sidebands, are essential for generating the PDH error signal and locking the laser to the cavity resonance.

The beam is collimated using a C230TMD-B lens from Thorlabs and directed into the optical cavity following the path shown in Figure B.1. The carrier frequency $\nu$ is close to the the cavity resonance, while the near sidebands at $\nu \pm f_{\mathrm{mod}}$ are reflected back due to their detuning from the cavity modes. This difference is key to generate the PDH error signal.

The light reflected from the cavity is detected by a photodiode and the resulting signal is demodulated at the modulation frequency $f_{\mathrm{mod}}$. This demodulation isolates the interference term between the carrier and the near sidebands, producing an error signal that is proportional to the frequency detuning. The error signal crosses the zero point at the cavity resonance and has a linear response near this point, making it ideal for use in a feedback loop to stabilize the laser frequency.

Once the laser is locked to the cavity using the near sidebands, the same EOM can be used to generate far sidebands at higher modulation frequencies, enabling large frequency shifts of the laser. By applying an additional modulation frequency $f_{\text{shift}}$ to the EOM, sidebands at $\nu \pm f_{\text{shift}}$ are created. These far sidebands allow the laser frequency to be shifted by a few GHz, providing a wide tuning range without requiring additional optical components. This capability is particularly advantageous for experiments requiring precise control over large frequency ranges, as it eliminates the need for complex setups involving multiple acousto-optic modulators (AOMs). In total, only one fiber-coupled EOM and one double-pass AOM are required for tuning, locking, and power stabilization of the laser light.

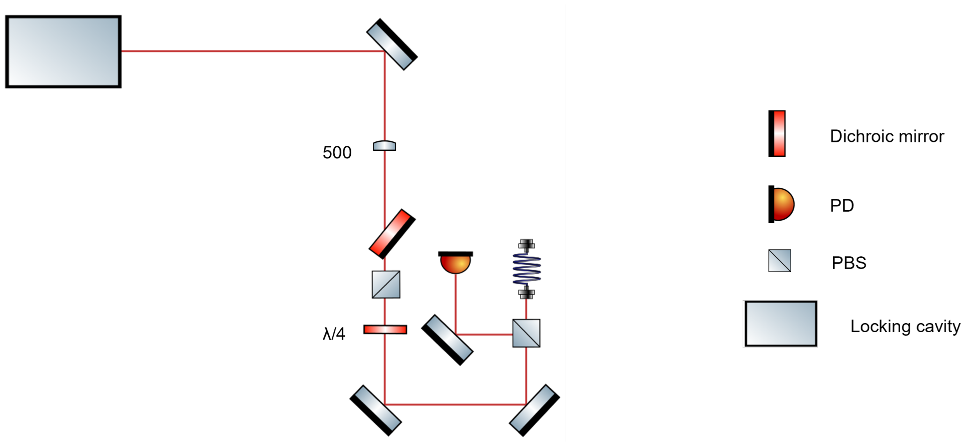

Figure B.1: Optical path of the 841 nm laser beam into the locking cavity.

Approximately 15 mW are going into the EOM fiber coupler. Unfortunately, the transmission of the EOM fiber is around 6% and so only 0.9 mW are used for laser locking. The fiber-coupled EOM modulates the sidebands at frequencies $f_{\text{mod}}$ and $f_{\text{shift}}$. The reflected beam from the cavity is intercepted with a polarizing beam splitter and recorded with a photodiode. The detected signal is mixed with the modulation frequency $f_{\text{mod}}$ to extract the PDH error signal.

The PDH error signal is generated by mixing the photodiode signal with the modulation frequency and applying a low-pass filter. The PDH error signal obtained with a modulation frequency $f_{\text{mod}}$ of 25 MHz is shown in Figure B.2. After locking the laser the error signal looks like the one shown in Figure B.3.

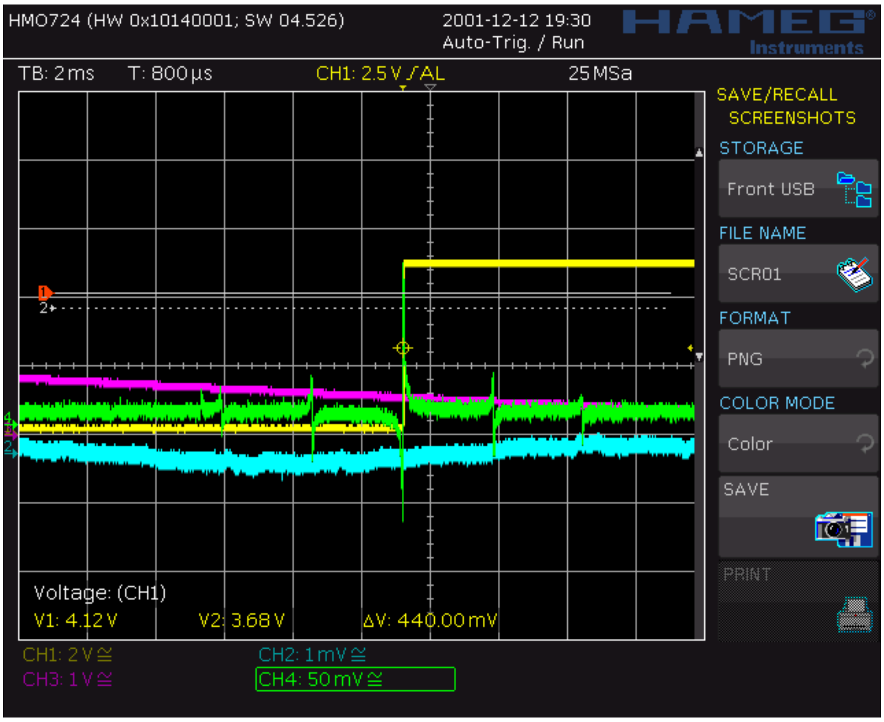
HMO724 (HW 0x10140001; SW 04.526)
2001-12-12 19:30
Auto-Trig. / Run
TB: 2ms T: 800µs CH1: 2.5V ⁄AL 25MSa
FILE NAME: SCR01
FORMAT: PNG
COLOR MODE: Color
STORAGE: Front USB
Voltage: (CH1)
V1: 4.12V V2: 3.68V ΔV: 440.00mV
CH1: 2V≅ CH2: 1mV≅
CH3: 1V≅ CH4: 50mV≅

Figure B.2: The PDH error signal is shown in green, illustrating the linear response near the cavity resonance.

To understand the behavior of the reflected beam from a FabryPerot cavity, we can analyze the electric field of the light at a point outside the cavity. The electric field of the incident beam can be expressed as:

$$E_{\text{inc}} = E_0 e^{i\omega t}, \tag{B.1}$$

where $E_0$ is the complex amplitude of the incident beam, and $\omega$ is the angular frequency of the light. Similarly, the electric field of the reflected beam is:

$$E_{\text{ref}} = E_1 e^{i\omega t}, \tag{B.2}$$

where $E_1$ is the complex amplitude of the reflected beam. The relative phase between the incident and reflected beams is encoded in the complex amplitudes $E_0$ and $E_1$.

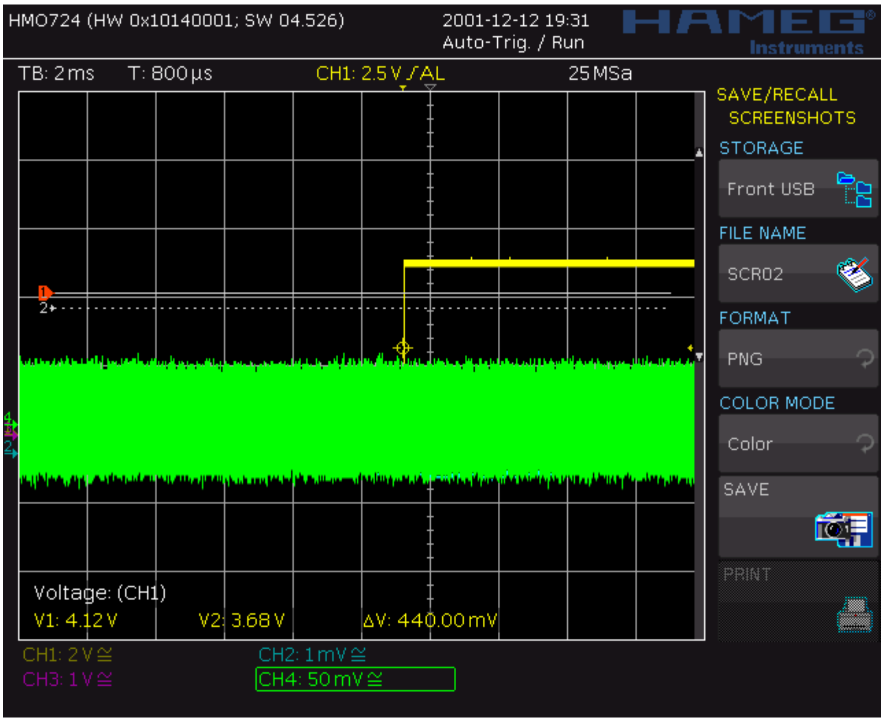

HMO724 (HW 0x10140001; SW 04.526)
2001-12-12 19:31
Auto-Trig. / Run
TB: 2 ms T: 800 µs CH1: 2.5 V /AL 25 MSa

STORAGE: Front USB
FILE NAME: SCR02
FORMAT: PNG
COLOR MODE: Color

Voltage: (CH1)
V1: 4.12 V V2: 3.68 V ΔV: 440.00 mV

CH1: 2 V≅ CH2: 1 mV≅
CH3: 1 V≅ CH4: 50 mV≅

Figure B.3: In green the PDH error signal when the laser is locked.

The reflection coefficient $F(\omega)$ is defined as the ratio of the reflected and incident electric fields:

$$F(\omega) = \frac{E_{\text{ref}}}{E_{\text{inc}}}. \tag{B.3}$$

For a symmetric FabryPerot cavity with no losses, the reflection coefficient is given by:

$$F(\omega) = r\frac{e^{i\omega_{FSR}} - 1}{1 - r^2 e^{i\omega_{FSR}}}, \tag{B.4}$$

where $r$ is the amplitude reflection coefficient of each mirror, and $\omega_{FSR} = \frac{c}{2L}$ is the free spectral range (FSR) of the cavity, with $L$ being the cavity length and $c$ the speed of light.

The reflected beam from the FabryPerot cavity is the coherent sum of two components:

1. The *promptly reflected beam*, which is the portion of the incident light that reflects off the first mirror without entering the cavity.

2. The *leakage beam*, which is the small fraction of the standing wave inside the cavity that leaks back through the first mirror. This leakage occurs because the mirrors are not perfectly reflective.

The interference between these two components determines the total reflected beam. The phase of the reflected beam depends on whether the laser frequency is above, below, or at the cavity resonance. Measuring this phase is crucial for determining the frequency detuning of the laser relative to the cavity resonance. Indeed, if we look at the reflected beam signal on a photdiode, and we measure a certain value (see Figure B.4) of intensity, we don't know if we are above or below the cavity resonance.

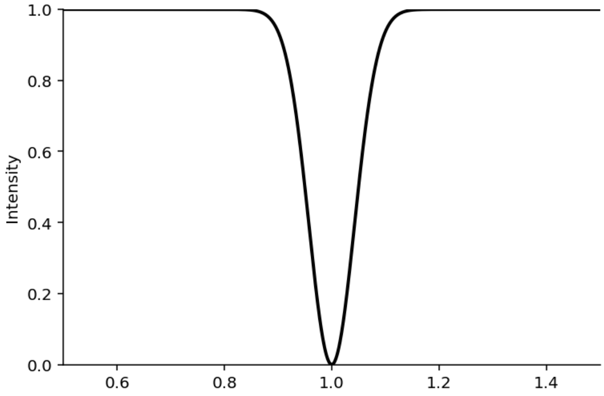

Figure B.4: Intensity of the beam reflected from the optical cavity. The minimum intensity corresponds to the cavity resonance, since the light will enter in the cavity, while if the laser frequency is not in resonance with a mode of the cavity, the beam is reflected from the first mirror and doesn't enter in the cavity.

Directly measuring the phase of a light wave is not feasible with current electronics. However, the PoundDreverHall (PDH) method provides an indirect way to measure the phase of the reflected beam by introducing sidebands through phase modulation.

The phase modulation is applied to the laser beam using an electro-optic modulator (EOM). After passing through the EOM, the electric field of the incident beam becomes:

$$E_{\text{inc}} = E_0 e^{i(\omega t + \beta \sin \Omega t)}, \tag{B.5}$$

where $\beta$ is the modulation depth, and $\Omega$ is the modulation frequency.

Using the expansion of the sinusoidal term in terms of Bessel functions, the modulated electric field can be written as:

$$E_{\text{inc}} \approx E_0 \left[ J_0(\beta) e^{i\omega t} + J_1(\beta) e^{i(\omega+\Omega)t} - J_1(\beta) e^{i(\omega-\Omega)t} \right], \tag{B.6}$$

where $J_0(\beta)$ and $J_1(\beta)$ are Bessel functions of the first kind. This expression shows that the modulated beam consists of three components:

- A *carrier* at the original frequency $\omega$,
- An *upper sideband* at frequency $\omega + \Omega$,
- A *lower sideband* at frequency $\omega - \Omega$.

The sidebands are generated with a well-defined phase relationship to the carrier. When the modulated beam reflects from the cavity, each frequency component interacts with the cavity differently, depending on its detuning from the cavity resonance. The total reflected electric field is:

$$E_{\text{ref}} = E_0 \left[ F(\omega) J_0(\beta) e^{i\omega t} + F(\omega+\Omega) J_1(\beta) e^{i(\omega+\Omega)t} - F(\omega-\Omega) J_1(\beta) e^{i(\omega-\Omega)t} \right], \tag{B.7}$$

where $F(\omega)$, $F(\omega+\Omega)$, and $F(\omega-\Omega)$ are the reflection coefficients for the carrier and the sidebands, respectively.

The power of the reflected beam, which is what we measure with a photodiode, is proportional to the square of the total electric field:

$$P_{\text{ref}} = |E_{\text{ref}}|^2. \tag{B.8}$$

After some algebra, the reflected power can be expressed as:

$$P_{\text{ref}} = P_c |F(\omega)|^2 + P_s \left[ |F(\omega+\Omega)|^2 + |F(\omega-\Omega)|^2 \right] + \text{interference terms}, \tag{B.9}$$

where $P_c$ is the power of the carrier, $P_s$ is the power of each sideband.

The interference terms oscillate at the modulation frequency $\Omega$ and contain information about the phase of the reflected carrier. These terms can be written as:

$$2\sqrt{P_c P_s}\Big[\mathrm{Re}\big\{F(\omega)F^*(\omega+\Omega) - F^*(\omega)F(\omega-\Omega)\big\}\cos(\Omega t) + \\ +\mathrm{Im}\big\{F(\omega)F^*(\omega+\Omega) - F^*(\omega)F(\omega-\Omega)\big\}\sin(\Omega t)\Big].$$

By mixing the photodetector signal with the modulation frequency $\Omega$ and applying a low-pass filter, we isolate the component of the signal that is proportional to the phase of the reflected carrier. This component is the PDH error signal, which crosses zero at the cavity resonance and has a linear response near this point. The resulting error signal is then optimized by adjusting the phase until the error signal has the desired antisymmetric shape as shown in Figure B.5.

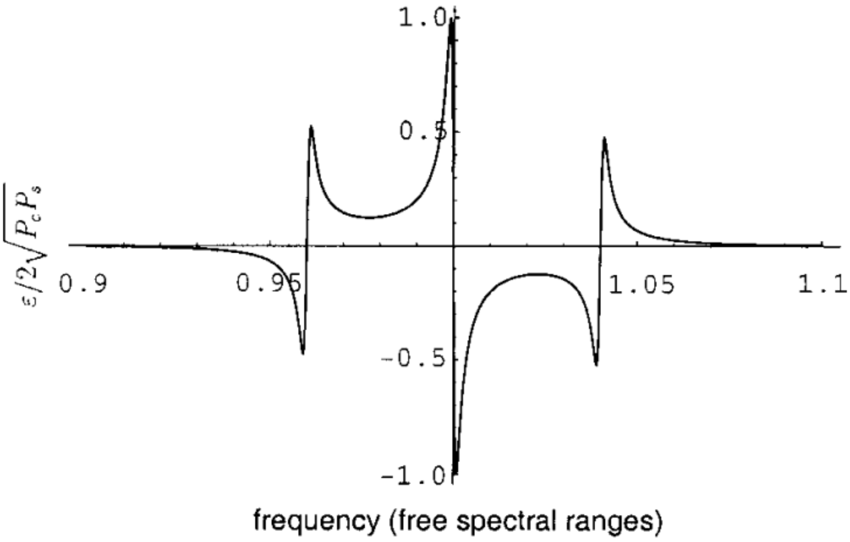

Figure B.5: PDH error signal.

Finally, the error signal is processed to stabilize the laser frequency as we will see in the next section.

## B.2 Implementation with Fast Servo Controller

We implement the PDH technique using a Fast Servo Controller from Moglabs. This device is essential for processing the error signal and providing real-time feedback to the laser. The Fast Servo Controller is designed to handle the high bandwidth required for stabilizing the laser frequency, compensating for fast fluctuations caused by environmental noise and intrinsic laser instabilities.

The error signal generated by the PDH scheme is fed into the Fast Servo Controller, which processes it using a proportional-integral-derivative (PID) control loop. The output of the controller is a voltage signal that is sent to the piezoelectric actuator of the laser. This voltage modulates the cavity length and so the laser frequency, ensuring that the laser remains locked to the cavity resonance.

The performance of the PDH locking system with the Fast Servo Controller is evaluated by monitoring the wavelength of the laser on the wavemeter. Considering a 40 MHz of uncertainty on the wavemeter, the laser wavelength looks very stable. The error signal slope, which determines the sensitivity of the locking system, has been optimized by adjusting the modulation depth and the PID parameters (knobs on the Fast Servo Controller). Figure B.6 and Figure B.7 show respectively the wavelength over time of the laser before and after locking.

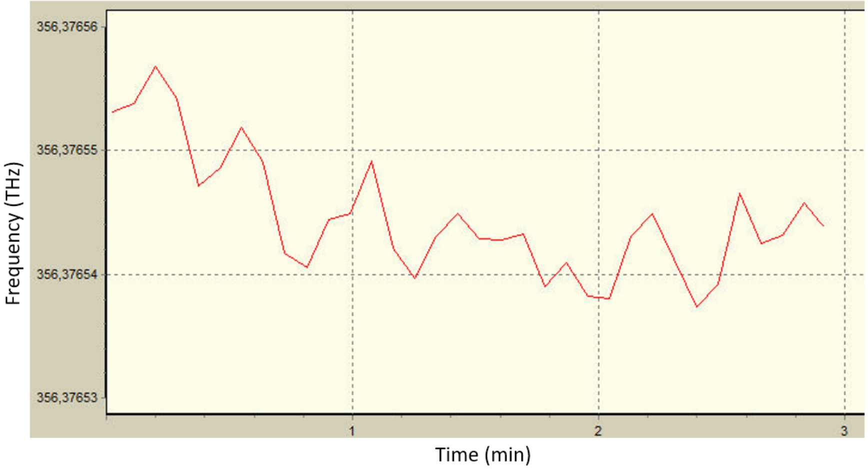

Figure B.6: Wavelength of the unlocked laser.

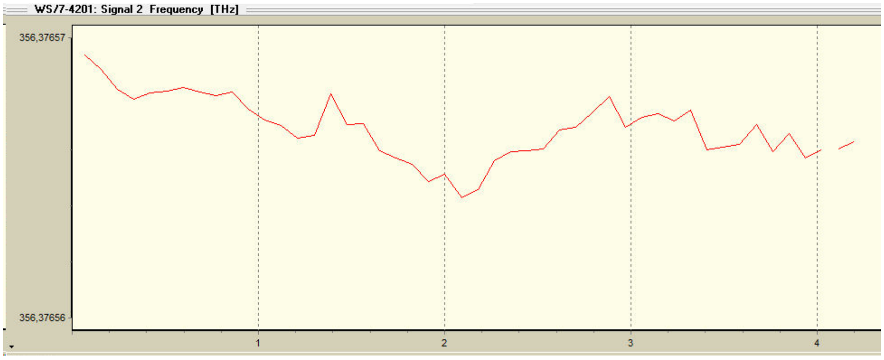

Figure B.7: Wavelength of the locked laser.

On the wavemeter we read the frequency that corresponds to 841.2238 nm vs time. We clearly see that in the case of the unlocked laser the fluctuations are around 10 MHz (last digit), while in the case of the locked laser the frequency is much more stable, less than 1 MHz of fluctuations.

The combination of the PDH technique and the Fast Servo Controller provides a robust and efficient solution for achieving ultra-stable laser frequency for our 841 nm laser.

# Bibliography

[1] Bose, S. N., *Plancks Law and the Hypothesis of Light Quanta*, Zeitschrift für Physik, 26, 178181, 1924. URL https://doi.org/10.1007/BF01327326.

[2] Einstein, A., *Quantentheorie des einatomigen idealen Gases*, Sitzungsberichte der Preussischen Akademie der Wissenschaften, 314, 1925.

[3] Cornell, E. A. and Wieman, C. E., *Nobel Lecture: BoseEinstein condensation in a dilute gas*, Reviews of Modern Physics, 74, 875893, 2002. URL https://doi.org/10.1103/RevModPhys.74.875.

[4] Anderson, M. H. et al., *Observation of BoseEinstein Condensation in a Dilute Atomic Vapor*, Science, 269(5221), 198201, 1995. URL https://doi.org/10.1126/science.269.5221.198.

[5] Davis, K. B. et al., *BoseEinstein Condensation in a Gas of Sodium Atoms*, Physical Review Letters, 75(22), 39693973, 1995. URL https://doi.org/10.1103/PhysRevLett.75.3969.

[6] Bradley, C. C. et al., *Evidence of BoseEinstein Condensation in an Atomic Gas with Attractive Interactions*, Physical Review Letters, 75(9), 16871690, 1995. URL https://doi.org/10.1103/PhysRevLett.75.1687.

[7] DeMarco, B. and Jin, D. S., *Onset of Fermi Degeneracy in a Trapped Atomic Gas*, Science, 285(5434), 17031706, 1999. URL https://doi.org/10.1126/science.285.5434.1703.

[8] Endres, M. et al., *Atom-by-atom assembly of defect-free one-dimensional cold atom arrays*, Science, 354(6315), 10241027, 2016. URL https://doi.org/10.1126/science.aah3752.

[9] Barredo, D. et al., *An atom-by-atom assembler of defect-free arbitrary 2D atomic arrays*, Science, 354(6315), 10211023, 2016. URL https://doi.org/10.1126/science.aah3778.

[10] Browaeys, A. and Lahaye, T., *Many-body physics with individually controlled Rydberg atoms*, Nature Physics, 16, 132142, 2020. URL https://doi.org/10.1038/s41567-019-0733-z.

[11] Labuhn, H. et al., *Tunable two-dimensional arrays of single Rydberg atoms for realizing quantum Ising models*, Nature, 534, 667670, 2016. URL https://doi.org/10.1038/nature18274.

[12] Bernien, H. et al., *Probing many-body dynamics on a 51-atom quantum simulator*, Nature, 551, 579584, 2017. URL https://doi.org/10.1038/nature24622.

[13] Scholl, P. et al., *Quantum simulation of 2D antiferromagnets with hundreds of Rydberg atoms*, Nature, 595, 233238, 2021. URL https://doi.org/10.1038/s41586-021-03585-1.

[14] Ebadi, S. et al., *Quantum phases of matter on a 256-atom programmable quantum simulator*, Nature, 595, 227232, 2021. URL https://doi.org/10.1038/s41586-021-03582-4.

[15] T. F. Gallagher, *Rydberg atoms*, Cambridge University Press, 1994.

[16] Löw, R. et al., *An experimental and theoretical guide to strongly interacting Rydberg gases*, Journal of Physics B: Atomic, Molecular and Optical Physics, 45(11), 113001, 2012. URL https://doi.org/10.1088/0953-4075/45/11/113001.

[17] Frisch, A. et al., *Narrow-line magneto-optical trap for erbium*, Physical Review A, 85(5), 051401(R), 2012. URL https://doi.org/10.1103/PhysRevA.85.051401.

[18] Aikawa, K. et al., *BoseEinstein Condensation of Erbium*, Physical Review Letters, 108(21), 210401, 2012. URL https://doi.org/10.1103/PhysRevLett.108.210401.

[19] Hansen, A. H. et al., *Quantum degenerate mixture of ytterbium and lithium atoms*, Physical Review A, 87(1), 013615, 2013. URL https://doi.org/10.1103/PhysRevA.87.013615.

[20] Metcalf, H. J. and van der Straten, P., *Laser Cooling and Trapping*, Springer, 1999. ISBN 978-0-387-98728-8.

[21] Chu, S., *Nobel Lecture: The manipulation of neutral particles*, Reviews of Modern Physics, 70(3), 685706, 1998. URL https://doi.org/10.1103/RevModPhys.70.685.

[22] J. Hennebichler, *Towards the creation of a two-dimensional optical tweezer array using a liquid crystal spatial light modulator*, Master Thesis, Innsbruck, November 2023.

[23] M. Saffman and T. G. Walker, *Quantum information with Rydberg atoms*, Revies of modern physics, volume 82, 2010. URL https://doi.org/10.1103/RevModPhys.82.2313

[24] D. S. Grün, S. J. M. White, et al., *Optical Tweezer Arrays of Erbium Atoms*, Phys. Rev. Lett. 133, 223402, 2024. URL https://doi.org/10.1103/PhysRevLett.133.223402

[25] M. Saffman, T. G. Walker, and K. Mølmer, *Quantum information with Rydberg atoms*, Rev. Mod. Phys. 82, 2313 (2010).

[26] Endres, M. et al., *Atom-by-atom assembly of defect-free one-dimensional cold atom arrays*, Science, 354, 1024, 2016. URL https://doi.org/10.1126/science.aah3752

[27] Cooper, A. et al., *Alkaline-earth atoms in optical tweezers*, Phys. Rev. X, 8, 041055 (2018). URL https://doi.org/10.1103/PhysRevX.8.041055

[28] Frisch, A. et al., *Quantum chaos in ultracold collisions of magnetic erbium atoms*, Nature, 507, 475 (2014). URL https://doi.org/10.1038/nature13137

[29] Madjarov, I. S. et al., *High-fidelity entanglement and detection of alkaline-earth Rydberg qubits*, Nat. Phys., 16, 857 (2020). URL https://doi.org/10.1038/s41567-020-0903-z

[30] Trautmann, A. et al., *Spectroscopy of Rydberg states in erbium using electromagnetically induced transparency*, Physical Review Research, 3(3), 2021. URL https://doi.org/10.1103/PhysRevResearch.3.033165.

[31] S. Embacher, *A new scanning optical dipole trap and towards optical potentials for erbium using q-plates*, Master Thesis, Innsbruck, November 2024

[32] D. S. Grün, L. Bellinato Giacomelli, et al., *Light-Assisted Collisions in Tweezer-Trapped Lanthanides*, arXive, 2025. URL https://doi.org/10.48550/arXiv.2506.05123

[33] A. El Arrach, *Characterisation of an Erbium Atomic Beam for Rydberg Experiments with Optical Tweezers*, Master Thesis, Innsbruck, April 2024

[34] D. A. Steck, *Quantum and Atom Optics*, available online at http://steck.us/teaching (revision 0.13.15, 28 July 2022).

[35] B. Liu et al., *Electric Field Measurement and Application Based on Rydberg Atoms*, Electromagnetic Science, vol. 1, no. 2, pp. 1-16, June 2023, Art no. 0020151, doi: 10.23919/emsci.2022.0015

[36] B. H. Bransden and C. J. Joachain, *Physics Of Atoms And Molecules*, 1983.

[37] A. Panja, et al., *Electric field control for experiments with atoms in Rydberg states*, arXive, 2024. URL https://doi.org/10.48550/arXiv.2409.11865

[38] Z. Lai, et al., *Polarizabilities of Rydberg states of Rb atoms with n up to 140*, Phys. Rev. A, 98, 052503 (2018). URL https://doi.org/10.1103/PhysRevA.98.052503

[39] D. Bloch, et al., *Trapping and imaging single dysprosium atoms in optical tweezer arrays*, Phys. Rev. Lett. 131, 203401 (2023). URL https://doi.org/10.1103/PhysRevLett.131.203401

[40] Hölzl, C. et al., *Motional ground-state cooling of single atoms in state-dependent optical tweezers*, Phys. Rev. Research 5, 033093, 2023. URL https://doi.org/10.1103/PhysRevResearch.5.033093

[41] D. M. Delmonego, *Building a Single-Frequency Diode Laser at 405 nm for Imaging of Potassium on the Blue Transition* , Master Thesis, Innsbruck, October 2020.

[42] A. Kramida, Yu. Ralchenko, J. Reader, and NIST ASD Team. *NIST Atomic Spectra Database (version. 5.10).* Gaithersburg, MD, 2016. URL https://dx.doi.org/10.18434/T4W30F. Accessed: 09/04/2025.

[43] E.D. Black, *An introduction to PoundDreverHall laser frequency stabilization.* Am. J. Phys. 69, 7987 (2001). URL https://doi.org/10.1119/1.1286663.

# Aknowledgments

At the end of this thesis work, I would like to thank all those who have stood by my side throughout my degree journey.

I would like to thank Professor Francesca Ferlaino for giving me the opportunity to work on a topic that has deeply fascinated me.

I would like to thank Professor Marco Barbieri for supporting me from the very first day of this work; his advice has been both helpful and greatly appreciated.

I would like to thank the members of the TREQS group, Daniel and Riccardo, for everything I have learned from you, and Arina for the first revisions of this work and for believing in me. I appreciated your support.

Ringrazio i miei genitori, che questa volta mi hanno supportato non solo moralmente, ma anche economicamente.

Ringrazio la mia famiglia, per essere sempre al mio fianco.

Ringrazio i miei compagni di università, a partire da Giulia, con la quale ho condiviso questi cinque anni di studi. Grazie a Matteo, Damiano, Davide ed Elena: la vostra amicizia è stata un punto di riferimento costante e una delle cose più belle di questo percorso.

Ringrazio Filippo, perché nonostante la distanza di questi ultimi anni, sarà sempre il mio Amico.

Infine, vorrei ringraziare Sofia: sei stata la novità più bella di questi mesi, e la tua presenza mi ha trasmesso grande serenità. Questa è solo la prima di tante sfide che affronteremo insieme.